

Physics Opportunities  
with  
 $e+A$  Collisions  
at an  
Electron Ion Collider

$e+A$  White Paper  
EIC Collaboration  
April 4, 2007

## DISCLAIMER

This report was prepared as an account of work sponsored by an agency of the United States Government. Neither the United States Government nor any agency thereof, nor any of their employees, nor any of their contractors, subcontractors, or their employees, makes any warranty, express or implied, or assumes any legal liability or responsibility for the accuracy, completeness, or any third party's use or the results of such use of any information, apparatus, product, or process disclosed, or represents that its use would not infringe privately owned rights. Reference herein to any specific commercial product, process, or service by trade name, trademark, manufacturer, or otherwise, does not necessarily constitute or imply its endorsement, recommendation, or favoring by the United States Government or any agency thereof or its contractors or subcontractors. The views and opinions of authors expressed herein do not necessarily state or reflect those of the United States Government or any agency thereof.

To the incoming virtual photon, the nucleus at very low  $x$  appears as a large wall of randomly oriented QCD color charge. The art on the cover is a depiction of a photon's eye view of the nucleus. Original photograph by John Chase: <http://www.flickr.com/photos/jahdakinebrah/301327284>. Additional manipulation by David Morrison and Thomas Ullrich.

# The EIC Collaboration\*

<sup>15</sup>C. Aidala <sup>8</sup>J. Annand, <sup>1</sup>J. Arrington, <sup>24</sup>R. Averbeck, <sup>3</sup>M. Baker, <sup>24</sup>K. Boyle <sup>26</sup>W. Brooks, <sup>26</sup>A. Bruell, <sup>17</sup>A. Caldwell, <sup>26</sup>J.P. Chen, <sup>2</sup>R. Choudhury, <sup>9</sup>E. Christy, <sup>7</sup>B. Cole, <sup>4</sup>D. De Florian, <sup>3</sup>R. Debbe <sup>24</sup>A. Deshpande, <sup>16</sup>K.Dow, <sup>24</sup>A.Drees, <sup>3</sup>J.C. Dunlop, <sup>2</sup>D. Dutta, <sup>26</sup>R. Ent, <sup>16</sup>R. Fatemi, <sup>16</sup>W. Franklin, <sup>26</sup>D. Gaskell, <sup>14</sup>G. Garvey, <sup>10</sup>M.Grosse-Perdekamp, <sup>1</sup>K. Hafidi, <sup>16</sup>D. Hasell, <sup>3</sup>T. Hemmick, <sup>1</sup>R. Holt, <sup>7</sup>E. Hughes, <sup>20</sup>C. Hyde-Wright, <sup>5</sup>G. Igo, <sup>12</sup>K. Imai, <sup>8</sup>D. Ireland, <sup>24</sup>B. Jacak, <sup>13</sup>P. Jacobs, <sup>26</sup>M. Jones, <sup>8</sup>R. Kaiser, <sup>15</sup>D. Kawall, <sup>9</sup>C. Keppel, <sup>6</sup>E. Kinney, <sup>16</sup>M. Kohl, <sup>2</sup>V. Kumar, <sup>15</sup>K. Kumar, <sup>19</sup>G. Kyle, <sup>11</sup>J. Lajoie, <sup>14</sup>M. Leitch, <sup>25</sup>J. Lichtenstadt, <sup>8</sup>K. Livingstone, <sup>18</sup>W. Lorenzon, <sup>13</sup>H. Matis, <sup>10</sup>N. Makins, <sup>16</sup>M. Miller, <sup>16</sup>R. Milner, <sup>2</sup>A. Mohanty, <sup>3</sup>D. Morrison, <sup>24</sup>Y. Ning, <sup>13</sup>G. Odyniec, <sup>11</sup>C. Ogilvie, <sup>2</sup>L. Pant, <sup>24</sup>V. Pantuyev, <sup>19</sup>S. Pate, <sup>24</sup>P. Paul, <sup>10</sup>J.-C. Peng, <sup>16</sup>R. Redwine, <sup>1</sup>P. Reimer, <sup>13</sup>H.-G.Ritter, <sup>8</sup>G. Rosner, <sup>23</sup>A. Sandacz, <sup>6</sup>J. Seele, <sup>10</sup>R. Seidl, <sup>8</sup>B. Seitz, <sup>2</sup>P. Shukla, <sup>13</sup>E. Sichtermann, <sup>16</sup>F. Simon, <sup>3</sup>P. Sorensen, <sup>3</sup>P. Steinberg, <sup>22</sup>M. Stratmann, <sup>21</sup>M. Strikman, <sup>16</sup>B. Surov, <sup>16</sup>E. Tsentalovich, <sup>9</sup>V. Tvaskis, <sup>3</sup>T. Ullrich, <sup>3</sup>R. Venugopalan, <sup>3</sup>W. Vogelsang, <sup>13</sup>H. Wieman, <sup>13</sup>N. Xu, <sup>3</sup>Z. Xu, <sup>7</sup>W. Zajc

<sup>1</sup>Argonne National Laboratory, Argonne, IL

<sup>2</sup>Bhabha Atomic Research Centre, Mumbai, India

<sup>3</sup>Brookhaven National Laboratory, Upton, NY

<sup>4</sup>University of Buenos Aires, Argentina

<sup>5</sup>University of California, Los Angeles, CA

<sup>6</sup>University of Colorado, Boulder, CO

<sup>7</sup>Columbia University, New York, NY

<sup>8</sup>University of Glasgow, Scotland, United Kingdom

<sup>9</sup>Hampton University, Hampton, VA

<sup>10</sup>University of Illinois, Urbana-Champaign, IL

<sup>11</sup>Iowa State University, Ames, IA

<sup>12</sup>University of Kyoto, Japan

<sup>13</sup>Lawrence Berkeley National Laboratory, Berkeley, CA

<sup>14</sup>Los Alamos National Laboratory, Los Alamos, NM

<sup>15</sup>University of Massachusetts, Amherst, MA

<sup>16</sup>MIT, Cambridge, MA

<sup>17</sup>Max Planck Institut für Physik, Munich, Germany

<sup>18</sup>University of Michigan Ann Arbor, MI

<sup>19</sup>New Mexico State University, Las Cruces, NM

<sup>20</sup>Old Dominion University, Norfolk, VA

<sup>21</sup>Penn State University, PA

<sup>22</sup>RIKEN, Wako, Japan

<sup>23</sup>Soltan Institute for Nuclear Studies, Warsaw, Poland

<sup>24</sup>SUNY, Stony Brook, NY

<sup>25</sup>Tel Aviv University, Israel

<sup>26</sup>Thomas Jefferson National Accelerator Facility, Newport News, VA

\*with valuable contributions from: <sup>11</sup>Alberto Accardi, Vadim Guzey (Ruhr-Universität Bochum, Germany), <sup>3</sup>Tuomas Lappi, <sup>3</sup>Cyrille Marquet, and <sup>11</sup>Jianwei Qiu.



### **Abstract**

We outline the compelling physics case for  $e+A$  collisions at an Electron Ion Collider (EIC). With its wide range in energy, nuclear beams, high luminosity and clean collider environment, the EIC offers an unprecedented opportunity for discovery and for the precision study of a novel universal regime of strong gluon fields in Quantum Chromodynamics (QCD). The EIC will measure, in a wide kinematic regime, the momentum and space-time distribution of gluons and sea-quarks in nuclei, the scattering of fast, compact probes in extended nuclear media and role of color neutral (Pomeron) excitations in scattering off nuclei. These measurements at the EIC will also deepen and corroborate our understanding of the formation and properties of the strongly interacting Quark Gluon Plasma (QGP) in high energy heavy ion collisions at RHIC and the LHC.



**Q**uantum Chromodynamics (QCD), the theory of strong interactions, is a cornerstone of the standard model of physics. Approximately 99% of the mass of baryonic matter in the universe can be attributed to QCD. This mass derives from “emergent phenomena” of the QCD vacuum that are not evident from the Lagrangian. These phenomena include chiral symmetry breaking and confinement that are fundamental features of the strong interactions.

Lattice gauge theory and effective field theories have taught us that the rich and complex structure of the QCD vacuum arises primarily from the dynamics of gluons with small contributions from the quark sea. Experiments probe the QCD vacuum in a variety of ways. In electron-positron annihilation, we observe the response of the vacuum to the deposition of enormous amounts of energy into minuscule space-time volumes. In hadron spectroscopy, we observe the way in which configurations of quarks and gluons carve out and inhabit bubbles in the vacuum. In relativistic heavy ion collisions, we observe the evolution of the vacuum after first heating a macroscopic ( $\gg 1$  fm) chunk of it to trillions of degrees Kelvin.

Precision measurements of deep inelastic scattering (DIS) of leptons with hadrons study properties of the QCD vacuum that are manifest in the structure of matter at resolution scales of less than a femtometer. DIS experiments with nuclei can identify those features of the short distance structure of matter which are common to all strongly interacting states. The kinematic invariants in fully inclusive DIS are the Bjorken variable  $x$ , the momentum transfer squared  $Q^2 > 0$ , the inelasticity  $y$  and  $s$ , the c.m. energy squared<sup>1</sup>. For fixed  $y$ ,  $x \propto Q^2/s$ ; thus high energies allow us to probe small values of  $x$ . DIS experiments of electrons off protons at the HERA collider at DESY have shown that, for  $Q^2 \gg \Lambda_{\text{QCD}}^2$  (where  $\Lambda_{\text{QCD}} \sim 200$  MeV), the gluon density grows rapidly with decreasing  $x$ . For  $x < 0.01$  the proton wave function is predominantly gluonic. DIS experiments with nuclei have established that quark and gluon distributions in nuclei exhibit shadowing; they are modified significantly relative to their distributions in the nucleon wave function. However, in sharp contrast to the proton, the gluonic structure of nuclei is not known for  $x < 0.01$ . The nature of gluon shadowing is *terra incognita* in QCD at high energies.

We will discuss in the following how an Electron Ion Collider (EIC) can enhance our understanding of universal features of the dynamics of gluons in nuclei.

At large  $x$  and at large  $Q^2$ , the properties of quarks and gluons in the hadron are well described by the linear evolution equations of perturbative QCD (pQCD). The rapid growth in gluon densities with decreasing  $x$  is understood to follow from a self similar Bremsstrahlung cascade where harder (large  $x$ ) parent gluons successively shed softer daughter gluons. Gluon saturation is a simple mechanism for nature to tame this growth. When the density of gluons becomes large, softer gluons can recombine into harder gluons. The competition between linear QCD Bremsstrahlung and non-linear gluon recombination causes the gluon distributions to saturate at small  $x$ . The onset of saturation and the properties of the saturated phase are characterized by a dynamical scale  $Q_s^2$  which grows with increasing energy (smaller  $x$ ) and increasing nuclear size  $A$ .

The nucleus is an efficient **amplifier** of the universal physics of high gluon densities. Simple considerations<sup>2</sup> suggest that  $Q_s^2 \propto (A/x)^{1/3}$ . Therefore DIS with large nuclei probes the same universal physics as seen in DIS with protons at  $x$ 's at least two orders of magnitude lower (or equivalently an order of magnitude larger  $\sqrt{s}$ ). Fig. 1 shows the saturation scale for protons and nuclei as a function of  $x$  in relation to the kinematic reach in  $x$  and  $Q^2$  of EIC. When  $Q^2 \gg Q_s^2$ , one is in the well understood “linear” regime of QCD. For large nuclei there is a significant window at small  $x$  where  $Q_s^2 \gg Q^2 \gg \Lambda_{\text{QCD}}^2$  and where one is in the domain of strong non-linear gluon fields.

The intensity of the chromo-electric and chromo-magnetic fields in the strong gluon field regime is of order  $O(1/\alpha_s)$ , where the asymptotic freedom of QCD dictates that the fine structure constant  $\alpha_s(Q_s^2) \ll 1$ . These fields are therefore the strongest fields in nature! Remarkably, the weak coupling suggests that the onset and properties of this regime may be computed systematically in a QCD framework. The high occupation numbers of gluons ensures that their dynamics is classical and their piling up at a characteristic momentum scale ( $Q_s^A$ ) is reminiscent of a Bose–Einstein condensate. Further, kinematic arguments suggest that the time scales of in-

1. For a brief primer on DIS kinematics, we refer the reader to the text box on page 4

2. For an expanded discussion, see the text box on page 9.

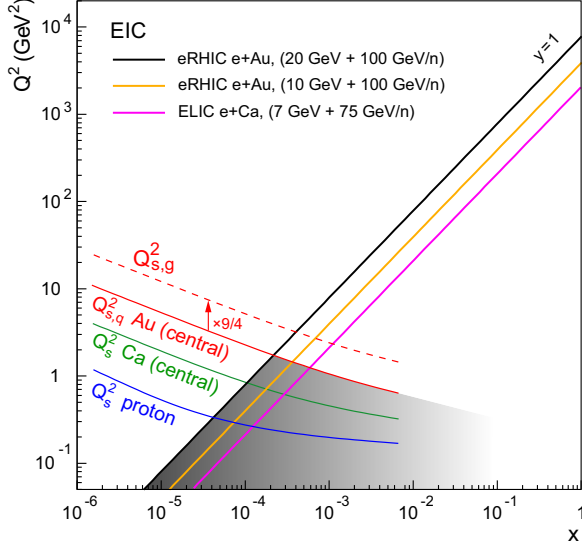


**Figure 1:** Kinematic acceptance in the  $(Q^2, x)$  plane for the EIC. Shown are lines for two complementary concepts to realize EIC, eRHIC and ELIC (see page 14 for details). Lines showing the quark saturation scale  $Q_s^2$  for protons, Ca, and Au nuclei are superposed on the kinematic acceptance. As indicated, the gluon saturation scale in Au nuclei is larger by the color factor  $9/4$ .

interactions of gluons are in practice time dilated well beyond characteristic time scales for gluon interactions. This slowing down is analogous to what happens in spin glasses. These dynamical and kinematic considerations have led to a suggestion that the matter in nuclear wave functions at high energies is universal and can be described as a Color Glass Condensate (CGC) [1, 2]. Alternative candidates for the appropriate degrees of freedom in QCD at high energies include color neutral excitations with vacuum quantum numbers called Pomerons. These come in soft (non-perturbative) or hard (perturbative) varieties [3]. A wide range of measurements with EIC, which we shall discuss shortly, can distinguish between predictions in the CGC (or other “unconventional” frameworks) and those following from the linear evolution equations of pQCD.

The nucleus is also a powerful **analyzer** of physics across the full range of  $x$ ,  $Q^2$  and  $A$ . In  $e+A$  collisions at high energies, the virtual photon mediating the interaction splits into a compact  $q\bar{q}$  “dipole” which scatters off the nuclear medium. The interaction of these fast, compact dipoles with an extended gluon medium provides insight into how partons lose energy, are absorbed, and how hadron formation is modified in the presence of a colored medium. Vary-

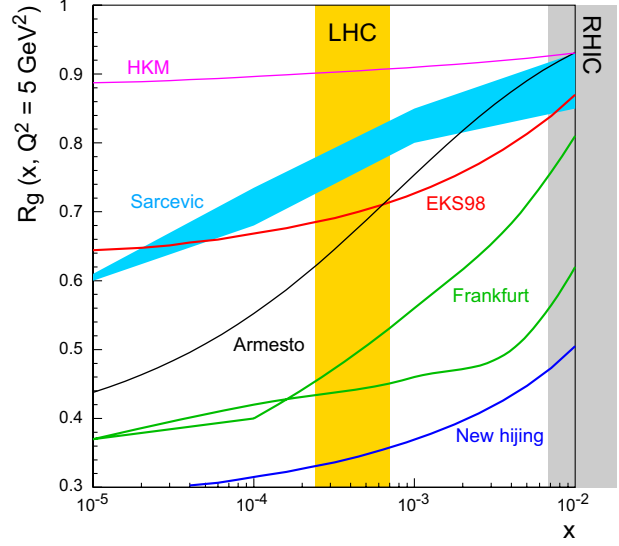


**Figure 2:** Ratios of the Pb over proton gluon PDFs versus  $x$  from different models at  $Q^2 = 5 \text{ GeV}^2$ . The RHIC and LHC ranges shown cover  $x = Q/\sqrt{s}$  at midrapidity. Figure taken from [4].

ing  $x$  and  $Q^2$  enables one to study the transparency or opacity of the medium relative to the propagation of the dipoles. We will discuss novel features of these studies that are made feasible by the EIC.

The physics of universal strong gluon fields as well as the response of compact probes in interactions with the gluonic medium are vital for a deeper understanding of the formation and thermalization of the strongly interacting Quark Gluon Plasma (QGP) currently being studied at RHIC and in the near future at the LHC. The plot shown in Fig. 2 illustrates this connection. Extrapolations of the gluon distribution in Pb nuclei to  $x$  values relevant for LHC energies differ by a factor of three. These correspond to an order of magnitude uncertainty in the cross-sections for semi-hard final states. As we shall demonstrate, measurements of the nuclear gluon distribution with EIC can strongly constrain these cross-sections.

We can study the properties of the gluon dominated region in nuclei by performing the measurements necessary to address the following questions:

- **What is momentum distribution of gluons (and sea quarks) in nuclei?**
- **What is the space-time distribution of gluons (and sea quarks) in nuclei?**

- What is the role of color neutral (Pomeron) excitations in scattering off nuclei?
- How do fast probes interact with an extended gluonic medium?

Some of these measurements have analogs in  $e+p$  collisions but have never been performed in nuclei; for these,  $e+A$  collisions will allow us to understand universal features of the physics of the nucleon and the physics of nuclei. Other measurements have no analog in  $e+p$  collisions and nuclei provide a completely unique environment to explore these.

In the next section we outline some of the measurements that will be made available with an Electron Ion Collider, and starting on page 12 we discuss connections of these with measurements in  $p+A$  collisions. We next discuss the relevance of specific measurements for heavy ion collisions. The final two sections sketch, respectively, the accelerator and detector concepts under consideration with emphasis on  $e+A$  physics measurements.

## Physics Program Overview

### The gluon momentum distribution

The fully inclusive structure functions  $F_2^A$  and  $F_L^A$  offer the most precise determination of quark and gluon distributions in nuclei. (A short discussion of these can be found in the text box on page 6.) The former is sensitive to the sum of quark and anti-quark momentum distributions in the nucleus; at small  $x$ , these are the sea quarks. The latter is sensitive to the gluon momentum distribution. Scaling violations of  $F_2^A$  ( $\partial F_2^A / \partial \ln(Q^2) \neq 0$ ) with  $Q^2$  are also sensitive to the gluon distribution  $G_A$  in the nucleus. In Fig. 3 we show projections from pQCD based models with differing amounts of shadowing and from a saturation (CGC) model for the normalized (per nucleon) ratio of  $F_2$ , in gold nuclei relative to the deuteron, compared to the statistical precision expected for an integrated luminosity<sup>3</sup> of  $4/A \text{ fb}^{-1}$  for 10 GeV electrons on 100 GeV/n Au nuclei<sup>4</sup> Fig. 3 shows that the quality of the data is sufficient to distinguish differing model predictions. The gluon distribution  $G_A$  can be extracted from the longitudinal structure function  $F_L^A$  which is directly proportional to the gluon distribution in the framework of pQCD. Independent extraction of  $F_2^A$  and  $F_L^A$  requires variation of the center of mass energy.

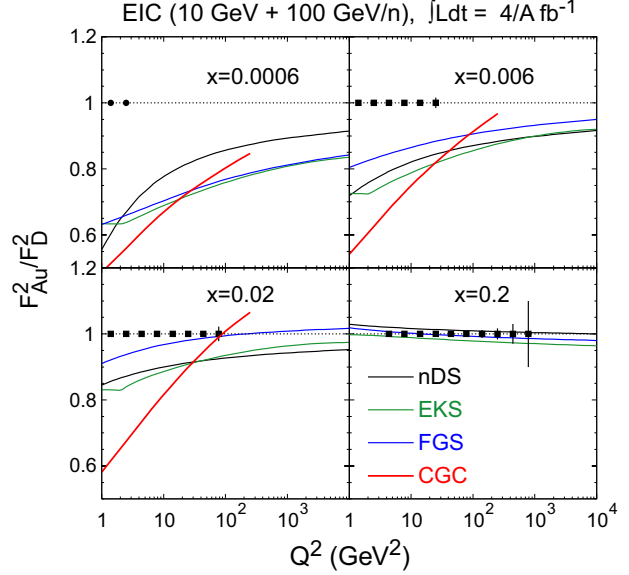


**Figure 3:** The ratio of the structure function  $F_2^{\text{Au}}$  in Au relative to the structure function  $F_2^{\text{D}}$  in the deuteron as a function of  $Q^2$  for several bins in  $x$ . The filled circles and error bars correspond respectively to the estimated kinematic reach in  $F_2$  and the statistical uncertainties for a luminosity of  $4/A \text{ fb}^{-1}$  with the EIC. Here the acronym nDS, EKS and FGS correspond to different parameterizations of parton distributions at the initial scale for pQCD evolution. The acronym CGC corresponds to a Color Glass Condensate model prediction applicable at small  $x$ .

In Fig. 5, the normalized (per nucleon) ratio of gluon distributions, in lead nuclei relative to the deuteron, extracted from the longitudinal structure is shown for  $10/A \text{ fb}^{-1}$  data for DIS on Pb nuclei. At small  $x$ , to good approximation,  $F_L^A / F_L^D \sim G_A / G_D$ . Existing world data on the gluon structure function is very sparse. The EIC will extend this kinematic range by at least an order of magnitude in  $x$  and significantly enhance the precision of our knowledge of gluon distributions.

We should note that the EIC, with luminosities of 100 higher than that achieved at HERA and a wide variability in center of mass energies can increase the precision of measurements of the gluon distributions even in the proton. This is particularly relevant for  $Q^2 < 10 \text{ GeV}^2$ , where there are significant uncertainties in the proton gluon distribution.

3. To good approximation the integrated luminosity decreases linearly with increasing  $A$ . We therefore quote the integrated luminosity in units of  $A$  where appropriate.

4. There are various notations common in the literature to indicate the beam energy per nucleon. We use  $\text{GeV}/n$ .

## Deep Inelastic Scattering

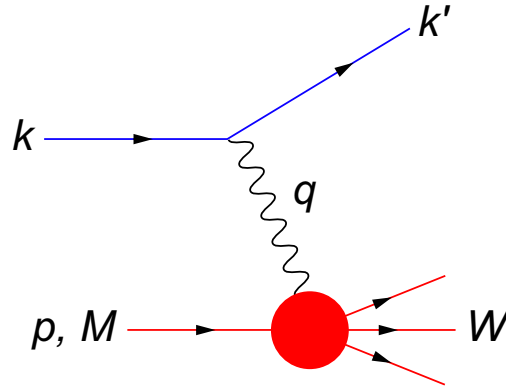


Figure 4: Kinematic quantities for the description of deep inelastic scattering. The quantities  $k$  and  $k'$  are the four-momenta of the incoming and outgoing lepton with mass  $m$ ,  $p$  is the four-momentum of a nucleon with mass  $M$ , and  $W$  is the mass of the recoiling system  $X$ . The exchanged particle is a  $\gamma$ ,  $W^\pm$ , or  $Z$ ; it transfers four-momentum  $q = k - k'$  to the nucleon.

High energy lepton-nucleon scattering plays a key role in determining the partonic structure of the nucleus (and nuclei). The process  $\ell(k) + N(p) \rightarrow \ell'(k') + X(p')$  is illustrated in Fig. 4. The filled circle in this figure represents the internal structure of a nucleon (in a nucleus) which can be expressed in terms of structure functions.

The following variables provide a relativistic-invariant formulation of the unpolarized inelastic electron-nucleon event kinematics:

$s = (k + p)^2 = \frac{Q^2}{xy} + M^2 + m^2 \approx 4E_\ell E_N$  is the square of the lepton-nucleon center of mass energy.

$x = \frac{Q^2}{2pq} = \frac{Q^2}{2M\nu}$  in the parton model, is the fraction of the nucleon or nucleus momentum carried by the struck parton. Note that for  $e+p$   $0 \leq x \leq 1$  while for  $e+A$  scattering  $0 \leq x \leq A$ .

$Q^2 = -(k - k')^2 = -q^2 \approx 4E_\ell E'_\ell \sin^2(\theta/2)$  where  $\theta$  is the lepton's scattering angle with respect to the lepton beam direction.  $Q^2$  is the negative square of the momentum transfer  $q$  and denotes the virtuality of the exchanged gauge boson. The momentum transfer  $q$  determines the size of the wavelength of the virtual boson and therefore the object size which can be resolved in the scattering process. Better resolution requires smaller wave lengths of the virtual boson and therefore larger momentum transfers.

$Q^2$  can be interpreted as the resolution power of the scatter. The maximum possible value for  $Q^2$  is given by  $Q_{\max}^2 = s$ .

$y = \frac{q \cdot p}{k \cdot p} = \frac{\nu}{E_\ell}$  is the fraction of the lepton's energy lost in the nucleon rest frame. It is thus also the fraction of the incoming electron energy (also known as inelasticity) carried by the exchange boson in the rest frame of the nucleon. In this case,  $y$  can also be written as  $\nu/\nu_{\max}$ . Note that  $0 \leq y \leq 1$ .

$\nu = \frac{q \cdot p}{M} = E_\ell - E'_\ell$  is the lepton's energy loss in the nucleon rest frame. Here,  $E_\ell$  and  $E'_\ell$  are the initial and final lepton energies in the nucleon rest frame. The maximum energy transfer  $\nu_{\max}$  is given by  $\nu_{\max} = s/2M$  which amounts to 4-5 TeV at the highest EIC energies.

$W^2 = (p + q)^2 = p'^2 = M^2 + \frac{1-x}{x}Q^2$  is the mass squared of the system  $X$  recoiling against the scattered lepton.  $W$  can also be interpreted as the center-of-mass energy of the gauge boson nucleon system. Small values of  $x$  correspond to large values of the invariant mass  $W$ .

The relativistic invariant variables  $x$ ,  $y$ ,  $Q^2$ , and  $s$  are connected through the following relation:  $Q^2 \simeq sxy$  where electron and nucleon masses have been ignored.

The process in Fig. 4 is called deep ( $Q^2 \gg M^2$ ) inelastic ( $W^2 \gg M^2$ ) scattering (DIS).

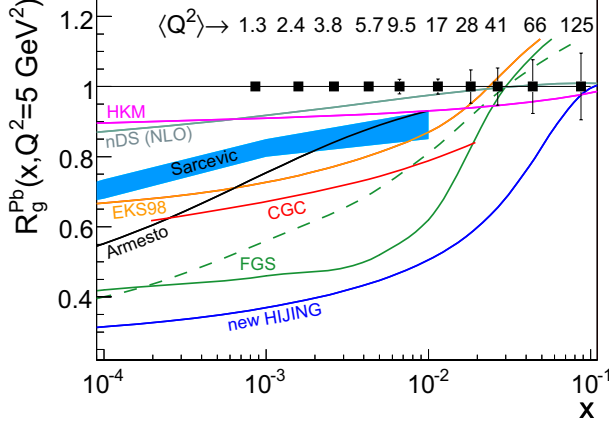


**Figure 5:** The ratio of gluon distributions in Pb nuclei to those in deuterium extracted from the ratio of the respective longitudinal structure functions  $F_L$ . The filled squares and error bars correspond respectively to the projected kinematic reach and statistical uncertainties for this measurement (for  $10/A \text{ fb}^{-1}$ ) with the EIC. A large range of model predictions are shown which differ widely in this kinematic region.

Measurements of the charm structure functions  $F_2^C$  and  $F_L^C$  are sensitive to the photon-gluon fusion process at high energies and will provide first data on nuclear charm quark distributions at  $x < 0.1$ . The high luminosities of EIC give estimates of  $10^5$  charm pairs for  $5 \text{ fb}^{-1}$  enabling precision charm studies. In Fig. 6, we show the  $p_\perp$ ,  $x$ , pseudo-rapidity  $\eta$  and  $Q^2$  distributions from the pQCD computations of Ref. [5] for  $e+p$  DIS compared to the kinematic range and integrated luminosities for 20 weeks of peak running at HERA and the EIC. The factor 100 higher luminosity allows us to test model predictions in a much wider kinematic range in  $e+p$  collisions at the EIC relative to HERA even though the c.m. energies (in  $e+p$ ) are three times smaller. Charm measurements in most of this kinematic range are unavailable in nuclei, so measurements in nuclei of the distributions in Fig. 6 will provide qualitatively new information of charm quark formation and propagation in nuclei. In the sections beginning on page 10 and also on page 13, we will discuss the physics that can be learned from heavy quark measurements in  $e+A$  DIS and the possible implications for heavy quark probes in heavy ion collisions. We note that inclusive charm measurements at  $x > 0.3$  are sensitive to the intrinsic charm component in nuclei which dominates conventional (photon-gluon fusion) charm production mechanisms in this kinematic region [8].

The photon-gluon fusion process results in semi-

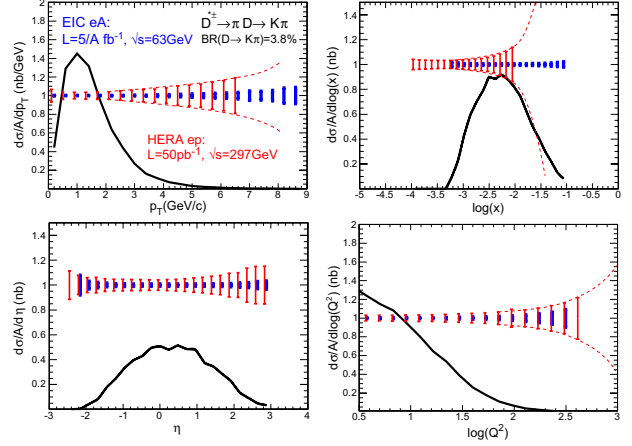


**Figure 6:** Predictions for the distributions of charm mesons as a function of  $p_\perp$ ,  $x$ , pseudo-rapidity  $\eta$ , and  $Q^2$  in a pQCD computation [5] compared to the kinematic range and statistical precision at HERA and EIC. The integrated luminosities correspond to 20 weeks of running at peak luminosity at the two colliders respectively. The errors for HERA shown are consistent with those published [6, 7]. The dot-dashed lines guide the projected divergence of the statistical errors at HERA at the stated integrated luminosity.

inclusive final states that are sensitive to the nuclear gluon distributions. Noteworthy examples are dijets channels. In the latter case, the QCD Compton process also contributes. For further discussion in the context of  $e+A$  studies, see Ref. [9].

Measurements of elastic vector meson production  $e+A \rightarrow (\rho, \phi, J/\psi)+A$  and Deeply Virtual Compton Scattering (DVCS)  $e+A \rightarrow e+A + \gamma$  are extremely sensitive to the momentum distribution of gluons in nuclei. The ratio, in a nucleus relative to the nucleon, of the forward cross-section for longitudinally polarized photons, is proportional in pQCD to the corresponding ratio of gluon distributions squared [10]. The  $Q^2$  dependence changes significantly in the non-linear saturation regime from  $1/Q^6$  to  $1/Q^2$  [11]. As we shall discuss further in the next section, measurements of exclusive final states are also very important for extracting the space-time distributions of glue.

## Cross-Sections and Structure Functions

For  $Q^2 < M_Z^2$ , where  $M_Z$  is the Z boson mass, the cross sections for deep inelastic scattering on unpolarized nucleons in Born approximation can be written in terms of the structure functions in the generic form:

$$\frac{d^2\sigma}{dx dQ^2} = \frac{4\pi\alpha^2}{xQ^4} \left[ \left(1 - y + \frac{y^2}{2}\right) F_2(x, Q^2) - \frac{y^2}{2} F_L(x, Q^2) \right]$$

The structure function  $F_2$  is sensitive to the sum of quark and anti-quark momentum distribution in the nucleon. The longitudinal structure function  $F_L = F_2 - 2xF_1$  starts to contribute to the cross-section at larger values of  $y$  but is negligible at very small  $y$  values. In the parton model,  $F_L = 0$ , while in QCD, it is directly proportional to the gluon structure function,  $F_L(x, Q^2) \propto \alpha_S x G(x, Q^2)$ , at low  $x$ .

The double-differential cross-section and therefore the event rate increases for  $Q^2 \rightarrow 0$  and  $y \rightarrow 0$ . The kinematic variable  $y$  is given by:  $y \approx 1 - E'_\ell/E_\ell$ . The limit  $y \rightarrow 0$  is therefore equivalent to  $E'_\ell \rightarrow E_\ell$ . The measured energy distribution of the scattered lepton at low  $Q^2$  is expected to exhibit a characteristic peak at the lepton beam energy  $E_\ell$ .

The figure shows the world data on the proton  $F_2$  as a function of  $Q^2$  for a wide range of fixed values of  $x$ . Knowledge on  $F_L$  is rather limited since it requires measurements at varying  $\sqrt{s}$ .

Besides the above expression for the differential  $e+N$  cross-section in terms of the structure functions  $F_1$  and  $F_2$  (or  $F_2$  and  $F_L$ ), one can interpret the cross-section as the product of a flux of virtual photons and the total cross-section  $\sigma_{tot}^{\gamma^*N}$  for the scattering of virtual photons on nucleons. This separation is only valid if the virtual photon state is coherent over times large compared to the time it takes to interact with the nucleus. The cross-section can now be written as the sum of the cross-section of transversely and longitudinally polarized photons.

$$\begin{aligned} \sigma_{tot}^{\gamma^*N} &= \sigma_T + \sigma_L \\ \sigma_T &= \frac{4\pi^2\alpha}{MK} F_1 \\ \sigma_L &= \frac{4\pi^2\alpha}{K} \left[ \left(1 + \frac{Q^2}{4x^2M^2}\right) \cdot \frac{2xM}{Q^2} F_2 - \frac{1}{M} F_1 \right] \\ &\approx \frac{4\pi^2\alpha}{2xMK} F_L \end{aligned}$$

where  $K$  is the flux factor  $K = \nu - Q^2/2M$ . The last equation motivates why  $F_L$  is called the longitudinal structure function.  $F_L$  is bounded to be in the range of  $0 \leq F_L \leq F_2$ . At small values of  $x$  the total cross-section can be written as:

$$\sigma_{tot}^{\gamma^*N} \approx \frac{4\pi^2\alpha}{Q^2} F_2(x, Q^2).$$

The apparent scaling of the data with  $Q^2$  at large  $x$  in early DIS data from SLAC was termed "Bjorken scaling" and motivated the parton model. Very strong violations of this scaling, as predicted by pQCD, can be seen at small  $x$  in Fig. 7.

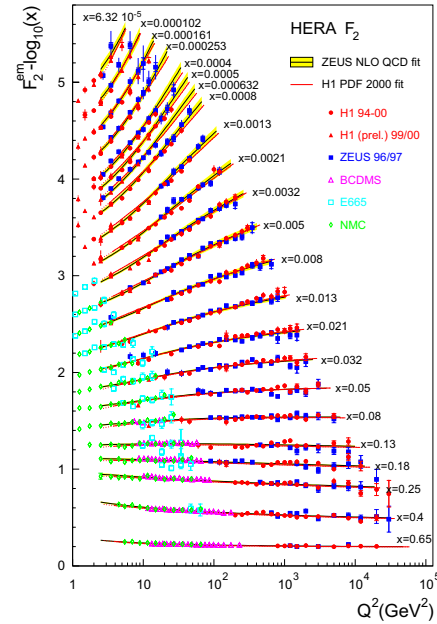


Figure 7: World data on the proton structure function  $F_2$  as a function of  $Q^2$  for fixed values of  $x$ .

## The gluon space-time distribution

Much of our knowledge of the distribution of gluons is with regard to their momentum distributions. How is the glue distributed spatially in hadrons and nuclei? In the latter, we would like to know if the “gluon density profile” in the nucleus in the transverse impact parameter plane is one of small clumps of glue or if its more uniform in impact parameter. The nature of the spatial distribution of glue provides a unique handle on the physics of high parton densities and has important ramifications for a wide range of final states in hadronic and nuclear collisions.

How do we extract information about the spatial distribution of glue? The physics of DIS at small  $x$  can be simply visualized in a frame where the virtual photon fluctuates into a quark anti-quark dipole that subsequently scatters coherently on the hadron or nucleus. Combined use of the predictions of this dipole picture for a) total cross-sections and b) the differential cross-section for the production of vector mesons, enables one to estimate the differential cross-section for the dipole to scatter elastically. The Fourier transform of the vector meson cross-section, as a function of the momentum transfer  $t$  along the proton line, allows one to estimate the scattering matrix for this amplitude. The optical theorem is then employed to extract the *survival probability* of small sized dipoles of size  $d \ll 1$  fm to propagate through the target at a given impact parameter  $b$  without interacting.

In pQCD, the survival probability of small sized dipoles is close to 1. This pQCD prediction should be contrasted with the survival probability in Fig. 8 extracted from dipole models. The Munier et al. [12] curves correspond to results from the elastic production of  $\rho_0$  mesons. HERA data for this process are limited and the curves result from differing extrapolations to large  $t$  or small impact parameters. The Rogers et al. [13] curve uses data on elastic  $J/\psi$  production allowing reliable extrapolation to lower impact parameters; the agreement at large  $b$  of these models is within 5%. At  $b = 0$ , the survival probability of dipoles can be as low as 20% suggesting very strong gluon fields localized at the center of the proton. A systematic dilution of the interaction strength (color transparency) is seen for larger  $b$ . Similar analyses for large nuclei give the survival probability of small sized ( $d = 0.3$  fm) dipoles from 60% at  $x = 10^{-2}$  to as low as 10% at  $x = 10^{-3}$ .

Estimates of the quark saturation scale [14,15]

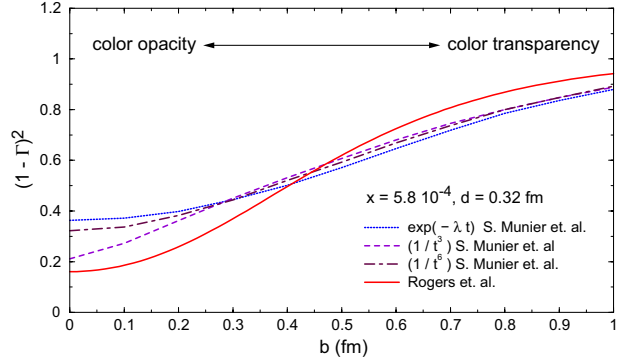


**Figure 8:** The survival probability  $(1 - \Gamma)^2$  of vector mesons as a function of impact parameter  $b$ , extracted from HERA data on elastic vector meson production on the proton. The Munier et al. curves are results extracted from data on  $\rho^0$  production in a limited region of momentum transfer  $t$  in the proton direction (see text). The Rogers et al. curve is for results extracted from  $J/\psi$  production.

extracted from the survival probability fit to data are shown in the left panel of Fig. 9. Results are shown for two saturation model parameterizations. In the right panel, the distribution of impact parameters contributing to the dipole cross-section is shown. The cross-section is dominated by median  $b \sim 0.4$  fm, corresponding to rather small values of the saturation scale. Therefore saturation effects are difficult to isolate for many processes in DIS off protons at present energies.

In contrast, the  $b$  profile of nuclei is much more uniform. The  $A$  dependence of the saturation scale can be determined by convoluting the gluon impact parameter profile in the proton with the nuclear density profile to fit the available inclusive *nuclear* (structure function) data from fixed target experiments. As shown in Fig. 1, there is a significant enhancement in the saturation scale at  $b = 0$  in the nucleus<sup>5</sup> relative to that in the proton for the median  $b = 0.4$  fm. A saturation model fit of HERA and NMC *inclusive* data to determine the  $A$ -dependence in large nuclei relative to light nuclei gives a nuclear enhancement of  $A^{0.38}$  [16] which is approximately 10% larger than the back of the envelope estimate of  $A^{1/3}$ . (See the text box on page 9 for further discussion.) First measurements of elastic vector meson final states at small  $x$  in nuclei will provide sensitive tests of the  $A$ -dependence of the saturation scale.

5. In large nuclei, the saturation scale for the “median”  $b$  value is close to the value at  $b = 0$ . The situation is very different in the proton as evident from Fig. 9.

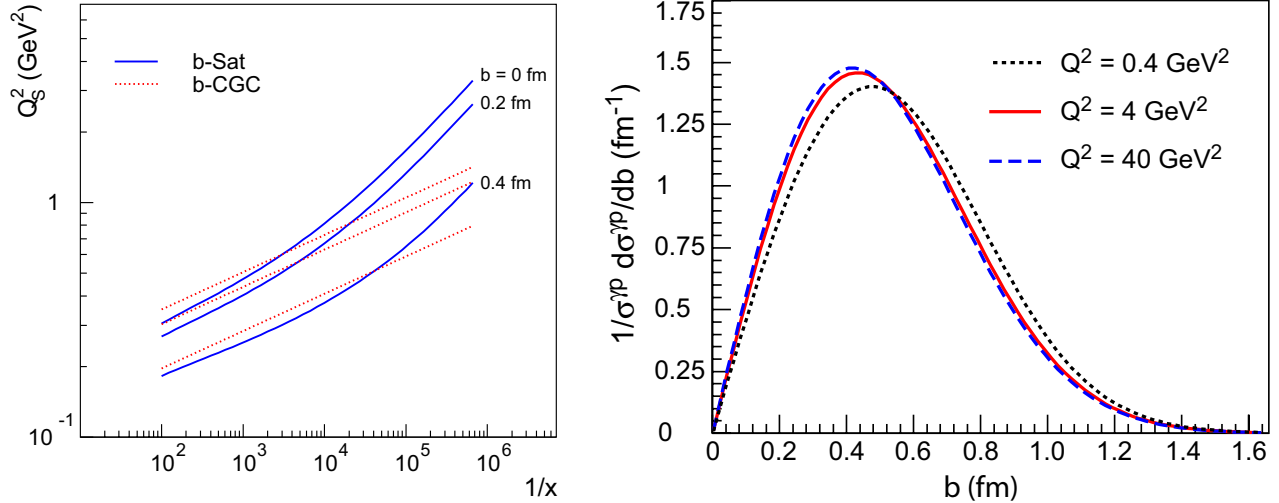


**Figure 9:** Left: The  $b$ -dependent saturation scale in the proton as a function of  $1/x$  extracted from two saturation model fits to the HERA data [14, 15]. Right: The dipole scattering cross-section off the nucleon is dominated by large  $b$ 's.

Deeply Virtual Compton Scattering (DVCS) on nuclear targets ( $e + A \rightarrow e + A + \gamma$ ) provides detailed information on the distribution and correlation of partons in nuclei (a 3D picture). Extracting information on DVCS is difficult because it interferes with the electromagnetic Bethe-Heitler process. However, in the 10 GeV+100 GeV/n EIC kinematics, DVCS dominates Bethe-Heitler for a wide range of nuclei (from  $^{40}\text{Ca}$  to  $^{208}\text{Pb}$ ); for example, for  $Q^2 = 3 \text{ GeV}^2$  and  $x \geq 0.02$ . This choice of kinematics allows clean studies of the nuclear DVCS amplitude (mostly its imaginary part) in the interesting transition region from nuclear shadowing to anti-shadowing. The integrated DVCS cross section is expected to increase as  $A^{4/3}$  (see below). Another possibility would be to study the imaginary and real parts of the nuclear DVCS amplitude via the beam-spin and beam-charge (azimuthal) asymmetries, respectively, in the kinematics, when  $Q^2$  is a few  $\text{GeV}^2$  and  $0.001 < x < 0.1$ . The former does not have a significant  $x$  or  $A$ -dependence while the latter is expected to have very rapid  $x$ -dependence and a significant  $A$ -dependence [17–20].

Coherent (nucleus stays intact) and incoherent (nucleus excites or breaks up) contributions are both important in nuclear DVCS [21]. The coherent contribution is concentrated at small  $t$  and dies rapidly away as  $F_A(t)^2$  ( $F_A(t)$  is the nuclear form factor); the incoherent cross section is proportional to  $F_N(t)$  ( $F_N(t)$  is the nucleon e.m. form factor) and dominates at large  $t$ . The coherent DVCS cross section

in nuclei is proportional to the square of the off-forward gluon distribution per unit area. In the limit of Color Transparency (CT), this gives  $A^{2/3}$  times a factor of  $A^{2/3}$  from the area resulting in an  $A$ -dependence for coherent DVCS of  $A^{4/3}$ . In the Color Opacity (CO) limit, one gets a factor  $A^{2/3}$  less from the area; the coherent DVCS cross-section in this case goes as  $A^{2/3}$ . Incoherent DVCS, in contrast to coherent DVCS, is proportional to the gluon distribution per unit area, not its square. In the CT limit, multiplying with the area factor results in a linear  $A$  dependence for incoherent DVCS. In the CO limit, one again gets a factor  $A^{2/3}$  less thus changing the  $A$ -dependence of incoherent DVCS to  $A^{1/3}$ .

### Color neutral (Pomeron) excitations

Diffractive interactions result when the electron probe in DIS interacts with a color neutral vacuum excitation. This vacuum excitation, which in QCD may be visualized as colorless combination of two or more gluons, is often called the Pomeron. At HERA, an unexpected discovery was that 15% of the  $e+p$  cross-section is from diffractive final states. This is a striking result implying that a proton at rest remains intact one seventh of the time when struck by a 25 TeV electron. The effect is even more dramatic in nuclei. Several models of strong gluon fields in nuclei suggest that large nuclei are intact  $\sim 40\%$  of the time, nearly saturating the quantum mechanical black disk bound of 50%.

## Nuclear ‘‘Oomph’’ Factor

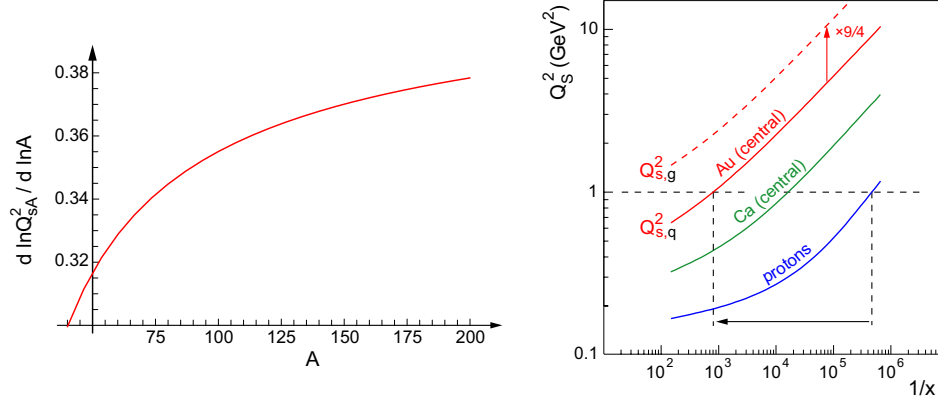


Figure 10: *Left: The  $A$  dependence of the saturation scale from the analysis of Ref. [16]. Right: The saturation scale at  $b = 0$  in Au and Ca nuclei compared to the median saturation scale in a proton [15].*

From the uncertainty principle, the interaction of an external QCD probe with a nuclear target of atomic number  $A$  develops over longitudinal distances  $l \sim 1/2m_N x$ , where  $m_N$  is the nucleon mass. When  $l$  becomes larger than the nuclear diameter ( $\sim A^{1/3}$ ), or equivalently when  $x \ll A^{-1/3}$ , the probe cannot distinguish between nucleons located on the front and back edges of the nucleus. All partons within a transverse area  $1/Q^2$ , determined by the momentum transfer  $Q$  across the target, participate in the interaction *coherently*. A probe of transverse resolution  $1/Q^2 \ll 1/\Lambda_{\text{QCD}}^2 \sim 1 \text{ fm}^2$  will experience large fluctuations of color charge proportional to the longitudinal extent of the nucleus along its path. The corresponding ‘‘kick’’ to the probe in a random walk through the nucleus is the saturation scale; one therefore expects  $(Q_s^A)^2 \propto A^{1/3}$ . The saturation scale also grows because the number of gluons in each nucleon along the probe’s path length increases with energy: a fit to HERA data based on the Golec-Biernat–Wusthoff (GBW) saturation model [22] gives  $(Q_s^p)^2 = Q_0^2 x^{-\delta}$ , where  $\delta \approx 0.3$  and  $Q_0^2$  is a non-perturbative scale in the proton. A simple pocket formula therefore to compare the saturation scale in heavy nuclei relative to the proton and in large nuclei relative to light nuclei is

$$(Q_s^A)^2 \approx c Q_0^2 \left(\frac{A}{x}\right)^{1/3}, \quad (1)$$

where  $c$  is a dimensionless constant. An analysis using the  $x$ -dependence of the GBW model and fits to NMC nuclear data also predicts the  $A$ -dependence of the saturation scale [16]. The result is shown in

the left panel of Fig. 10. The power is shown to be  $\approx 10\%$  larger than  $1/3$  in Eq. 1; the coefficient is estimated to be  $c \approx 0.5$  for large nuclei.

A more detailed analysis (going beyond the framework of the GBW model) of the  $x$  and  $A$  dependence of the saturation scale was performed by Kowalski and Teaney [15]. They extracted the  $b$  and  $x$  dependence of the saturation scale in the proton from fits to the diffractive and exclusive HERA data—see Fig. 9 in text. This  $b$ -dependent profile in the nucleon was then used to construct (using Glauber Monte Carlo methods) the  $b$  dependent quark saturation scale  $Q_s^A(x, b)$  in nuclei. Inclusive cross-sections in nuclei are simply related to this saturation scale and Kowalski and Teaney verified this result is consistent with NMC DIS data on nuclei. The quark saturation scale squared in Au and Ca nuclei relative to the proton is shown in the right panel of Fig. 10; the gluon saturation scale squared is larger by a color factor of  $9/4$ .

The nuclear profile of large nuclei is nearly constant out to large  $b$ ; that of the proton falls sharply. The median  $b$  for a proton is shown in the right panel of Fig. 9. As inclusive scattering is dominated by the median impact parameter, it is therefore appropriate to compare the saturation scales in the center of the nucleus to the median  $b$  in the proton, as shown in Fig. 10. The ‘‘oomph’’ factor of large nuclei is seen to be quite significant. Measurements extracting the  $x$ ,  $b$  and  $A$  dependence of the saturation scale provide very useful information on the momentum and space-time distribution of strong color fields in QCD at high energies [23].

In Fig. 11, we show results from a dipole model prediction of diffractive effects in nuclei [24]. The model<sup>6</sup> includes the effects of *linear* small  $x$  evolution for small dipoles ( $d < 1/Q_s$ ) and *saturation* effects for larger sized dipoles ( $d > 1/Q_s$ ). The latter can be turned off in the model and the curves (right panel) correspond to results with and without saturation effects. In the left panel, we see that the ratio of the diffractive to total structure function is large and grows by about 30% from light to heavy nuclei. Very significantly, even though the nuclei are intact, the diffractively produced final states are semi-hard with momenta  $\sim (Q_s^A)^2$ . They are therefore harder with increasing nuclear size. In the right panel, the normalized ratio of diffractive structure functions in heavy nuclei relative to light nuclei is shown as a function<sup>7</sup> of the fraction of the nuclear momentum carried by a Pomeron ( $x_{\mathbb{P}}$ ) and as a function of  $\beta$  defined as  $\beta = x/x_{\mathbb{P}}$ .

Saturation/strong gluon field models predict a weak  $x$  dependence and a strong  $Q^2$  dependence of these ratios. They should be clearly distinguishable from non-perturbative (“soft” Pomeron) models of diffractive scattering [25]. In the pQCD framework, factorization theorems exist for diffractive DIS; as in inclusive DIS, diffractive parton distributions are introduced at an initial hard scale and are evolved to harder scales with the DGLAP equations. As we will discuss later, these factorization theorems for diffractive PDFs do not extend to hadronic collisions, indicating the breakdown of factorization theorems for diffractive processes.

Model results suggest that multi-gluon correlations are enhanced in large nuclei. Can these be described in terms of universal quasi-particle degrees of freedom? Measurements of coherent diffractive scattering on nuclei are easier in the collider environment of EIC relative to fixed target experiments. These will provide definitive tests of strong gluon field dynamics in QCD. Preliminary studies indicate that such measurements are not statistics limited.

Diffractive measurements will be strongly systematics limited so simple qualitative model predictions such as those discussed here can be substantially affected when combined with the available acceptance for such measurements. Realistic simulations of diffractive final states are required to confirm that the qualitative differences between models can be distinguished with the acceptance of EIC.

## Hadronization and energy loss

In Deep Inelastic Scattering on nuclear targets (nDIS) one observes a suppression of hadron production [26–30] analogous to but weaker than the quenching in the inclusive hadron spectrum observed in heavy-ion collision at the Relativistic Heavy-Ion Collider (RHIC) [31]. The cleanest environment to address nuclear modifications of hadron production is nuclear DIS. It allows one to experimentally control many kinematic variables; the nucleons act as femtometer-scale detectors allowing one to experimentally study the propagation of a parton in this “cold nuclear matter” and its space-time evolution into the observed hadron. (See left panel of Fig. 12.)

Experimental data on hadron production in nDIS are usually presented in terms of the ratio [27–30] of the single hadron multiplicity per DIS event on a target of mass number  $A$  normalized to the multiplicity on a deuterium target. This ratio can be studied as a function of the virtual photon energy  $\nu$ , the virtuality  $Q^2$ , the hadron transverse momentum  $p_{\perp}$ , and  $z_h = p \cdot p_h / p \cdot q$ . ( $p$  is the target 4-momentum divided by  $A$ ,  $p_h$  the hadron 4-momentum and  $q$  the virtual photon 4-momentum.) In the target rest frame  $z_h = E_h/\nu$  is the fractional energy carried by a hadron with respect to the virtual photon energy. See Fig. 12 right.

The basic question to be answered is on what time scale the color of the struck quark is neutralized, acquiring a large inelastic cross-section for interaction with the medium.<sup>8</sup> Energy loss models [33–35] assume long color neutralization times, with “pre-hadron” formation outside the medium and parton energy loss as the primary mechanism for hadron suppression. Absorption models [32, 36–38] assume short color neutralization times with in-medium “pre-hadron” formation and absorption as the primary mechanism. There are indications for short formation times from HERMES data [28] and JLAB preliminary data [30]. As shown in the right panel of Fig. 12 however, more data for a wider energy range is needed to clearly distinguish between

6. The model does not include impact parameter dependence of the saturation scale in nuclei which can be expected to modify the results. However, because we consider ratios, the qualitative features illustrating the difference between linear and non-linear evolution will likely be robust.

7. See text box on page 15 for a brief primer on diffractive variables.

8. Measurements of hadronic final states in nuclei will also allow one to quantify the relative contribution of nuclear valence and sea quark distributions.

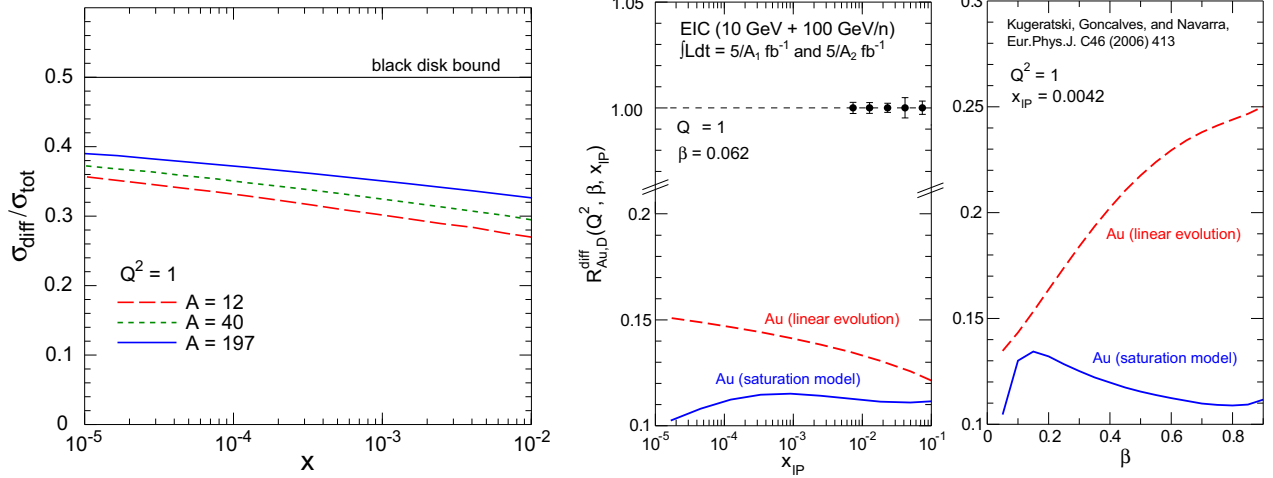


**Figure 11:** Left: A saturation model prediction [24] for the ratio of diffractive to total cross-sections as a function of  $x$  for fixed  $Q^2$  and several  $A$ . Right: The normalized ratio of diffractive structure functions in Au to deuterium nuclei is shown as a function of the variables  $x_{\text{IP}}$  and  $\beta$  at fixed  $Q^2$ ; the curves contrast model predictions of linear and non-linear QCD evolution effects. See text for details. The statistical uncertainties are negligible relative to model predictions for EIC luminosities.

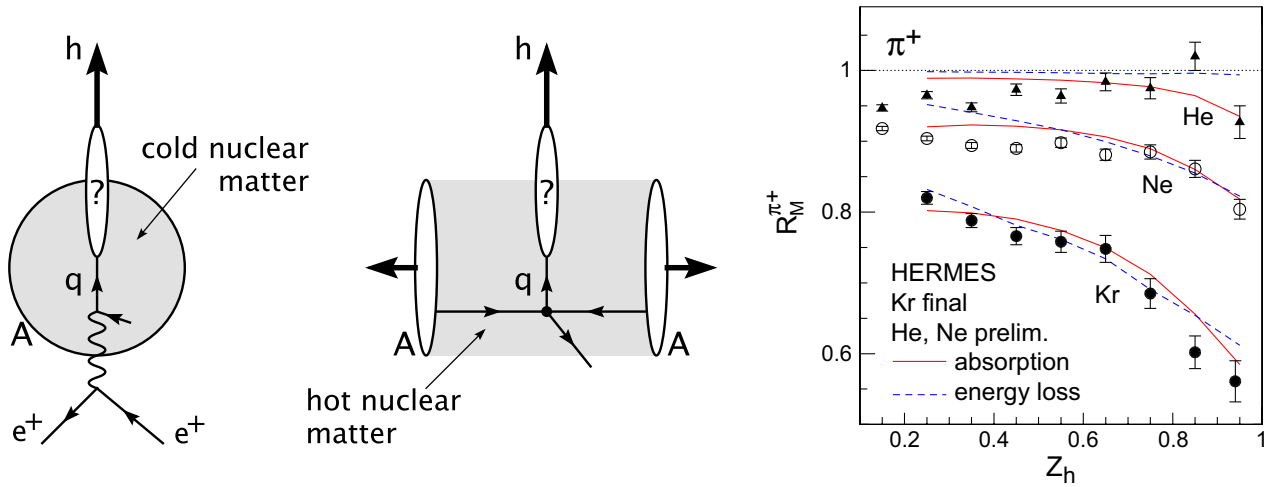


**Figure 12:** Left: In  $e+A$  collisions the hadronizing quark travels through the target nucleus. Center: In  $A+A$  collisions the hadronizing parton travels through the produced hot medium. Right: Ratio of  $\pi^+$  multiplicity in He, Ne and Kr to that in deuterium as measured by HERMES [28] and as compared to absorption model computations (solid) [32], and energy loss model computations (dashed) [33].

the models. At the EIC, the range of photon energies would be  $10 \text{ GeV} < \nu < 1600 \text{ GeV}$  compared to HERMES (2–25 GeV). It therefore offers more channels to study hadronization inside and outside of the nucleus and reaches into a region relevant for the LHC.

Further progress requires an increase in the statistical significance of the data to allow multi-differential measurements in all kinematic variables.

A novel feature of these studies at the EIC would be measurements providing insight into the energy loss and hadronization of heavy quarks to form *charm and bottom mesons*. Important measurements also include the study of baryon number transport in nuclei, nuclear modification of hadron  $p_{\perp}$  spectra and dihadron correlations to test and constrain hadronization mechanisms. All of these measurements (as we shall discuss in section 4) have analo-

gous measurements in heavy ion collisions. One can therefore in principle isolate hadronization effects in the “cold” vacuum from how hadronization is modified in a hot, excited vacuum.

The high luminosities of the EIC will allow access to rare signals and double differential measurements. Its high energies include and exceed most fixed target facilities to date and its excellent low  $x$  coverage provides increased production of heavy flavor (see section 2.2) and quarkonia. Finally, the collider kinematics and associated detectors with excellent hadron detection will allow for a comprehensive program to better understand how energy loss and hadronization occur in cold nuclear matter.

## Connection to $p+A$ Physics

Both  $p+A$  and  $e+A$  collisions can provide excellent information on the properties of gluons in the nuclear wave functions because it is unlikely that a hot dense hadronic medium would be produced at currently available  $p+A$  collision energies.

Deeply inelastic  $e+A$  collisions are dominated by one photon exchange; they have a better chance to preserve the properties of partons in the nuclear wave functions because there is no direct color interaction between  $e$  and  $A$ . The photon could interact with one parton to probe parton distributions, as well as multiple partons coherently to probe multiparton quantum correlations [39].

Many observables in  $p+A$  collisions require gluons to contribute at the leading order in partonic scattering. Thus  $p+A$  collisions provide more direct information on the response of a nuclear medium to a gluon probe. However, soft color interactions between  $p$  and  $A$  before the hard collision takes place has the potential to alter the nuclear wave function and destroy the universality of parton properties [40]. Such soft interactions contribute to physical observables as a correction at order  $1/Q^4$  or higher [41–43]. These power corrections cannot be expressed in terms of universal parton properties in the nuclear wave functions thereby breaking QCD factorization.

The breakdown of factorization has already been observed in comparisons of diffractive final states in  $e+p$  collisions at HERA and  $p+p$  collisions at the Tevatron. At HERA, diffractive parton distribution functions are extracted from fits to diffractive cross-section data; these diffractive pdf’s, used as input in a factorized approach to compute diffractive di-jet data at the Tevatron, overestimate the cross-section

by at least an order of magnitude. This result can be seen in Fig. 13. *One can therefore expect diffractive measurements in  $e+A$  collisions at EIC to be qualitatively different from those in  $p+A$  diffractive final states at the LHC.*

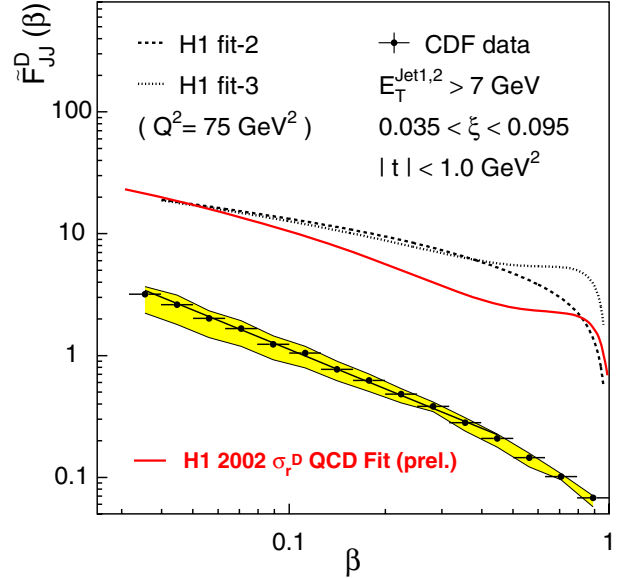


**Figure 13:** *Diffractive di-jet data in  $p+p$  collisions at the Tevatron (data points in yellow band) compared to curves showing predictions from fits to  $e+p$  diffractive structure function data [44]. The discrepancy between theory and experiment demonstrates strong breaking of factorization for diffractive final states.*

Due to the very large reach in  $x$  and  $M^2$ ,  $p+A$  collisions at the LHC have significant discovery potential for the physics of strong color fields in QCD. However, due to uncertainties relating to convolutions over parton distributions in the proton probe, final state fragmentation effects and factorization breaking contributions, the results can be cleanly interpreted only for  $M^2 \gg Q_s^2$  where the strong field effects will be weaker.<sup>9</sup> As discussed previously (see Fig. 1 and related text), saturation effects in the strong field regime of  $Q_s^2 > Q^2$  will be accessible in  $e+A$  collisions. Genuine discovery of the physics of this novel regime will require complementary hadronic and leptonic probes.

<sup>9</sup> Similar considerations will also complicate extraction of leading twist gluon distributions in nuclei.

## Connections to RHIC and LHC

Measurements over the last six years in heavy ion collision experiments at RHIC indicate the formation of a strongly coupled plasma of quarks and gluons (sQGP). Striking results include the strong collective flow of all mesons and baryons (of particular note is the strong flow even of heavy charm quarks) and the opaqueness of the hot and dense medium to hadron jets up to  $p_{\perp} \sim 20$  GeV. This sQGP behaves like a “near-perfect fluid” with a ratio of shear viscosity to entropy approaching zero [31,45]. To fully explore and quantify the properties of this system, upgrades of the collider and detectors at RHIC are planned.  $p+p$ ,  $p+A$  and  $A+A$  experiments at the LHC will provide substantially higher energies.

While evidence of collective behavior is compelling, there is still no quantitative framework to understand all the stages in the expansion of the hot and dense matter. We outline here how EIC can contribute to a better understanding of the dynamics of heavy ion collision—from the initial formation of partonic matter in bulk to jet quenching and hadronization that probe the properties of the sQGP.

**Initial Conditions for the sQGP** Understanding the dynamical mechanisms that lead to *rapid equilibration* in heavy ion collisions is perhaps the major outstanding issue of the RHIC program. Hydrodynamic modeling of RHIC data suggests that the system achieves nearly complete thermalization no later than  $1\text{ fm}/c$  after the initial impact of the two nuclei. These hydrodynamic models are very sensitive to the initial pre-equilibrium properties of the matter (often called “Glasma”) formed immediately after the collision of the two nuclei. The properties of these nuclear wave functions will be studied in great detail in  $e+A$  collisions. They therefore promise a better understanding of the initial state and its evolution into the sQGP. Specifically, the saturation scale  $Q_s$ , which can be independently extracted in  $e+A$  collisions, sets the scale for the formation and thermalization of strong gluon fields from the CGC wave functions [46–49]. Beyond establishing the multiplicity and initial energy density, these gluon fields may contribute to instability-driven thermalization [50]. To extract the parameters of the system’s evolution, the initial state of the system before hydrodynamic evolution must be known precisely: saturation effects may have a large impact on extracted hydrodynamic parameters[51].

Experiments at the EIC are crucial for the precise determination of the properties of the system at RHIC.

### Energy Loss and Hadronization in Hot Matter

The use of hard probes to study the properties of hot matter in heavy ion collisions is moving into the precision stage with high luminosities at RHIC and high energies at the LHC. The strong suppression of high  $p_T$  hadrons observed in RHIC collisions has a natural interpretation in terms of partonic energy loss via induced gluon radiation in the high-density matter. The initial parton distributions (which determine the incoming flux) play a crucial role in quantitatively extracting the amount of energy lost. These distributions are strongly modified in nuclei, with shadowing and saturation at low  $x$  and the EMC effect at moderate  $x$ . To calibrate the nuclear parton distributions,  $G_A(x, Q^2)$  must be well constrained for  $x \geq 10^{-2}$  at RHIC, and  $x \geq 10^{-4}$  at the LHC for  $Q^2 \sim 1\text{--}10\text{ GeV}^2$ . Fig. 2 shows that the current uncertainties, especially at the LHC, are large, leading to differences in the final transverse energy flow by factors of 2–4 and an order of magnitude uncertainty in semi-hard cross-sections[4]. At the same time, RHIC data on  $\pi^0$  production in deuteron-gold collisions at high  $p_{\perp}$  and on photon production in  $A+A$  collisions at high  $p_{\perp}$  suggest non-trivial modifications of parton distributions at  $x > 0.1$ . Precision measurements in the kinematic regime relevant to the RHIC measurements are essential for using hard probes to diagnose the active degrees of freedom of the sQGP.

While the RHIC data is broadly explained by the attenuation of quarks and gluons in a hot medium, quantitative studies require that the role of the cold nuclear medium on partons and hadrons be well understood. HERMES DIS data confirm that the energy loss and  $p_T$ -broadening of formed hadrons produced in  $e+A$  collisions are small, but the luminosity at HERMES is too low to study the attenuation of charm or bottom quarks. In hot matter at RHIC, the surprisingly large energy loss of heavy partons poses major challenges to theory [52]; conjectures about the role of collisional energy loss and pre-hadron absorption in the attenuation of heavy quarks can be tested, for the first time, in cold matter with EIC. Further, the wide range of photon energies at an Electron Ion Collider  $10\text{ GeV} < \nu < 1600\text{ GeV}$  compared to HERMES (2–25 GeV) offers more channels to study hadronization inside and outside of the nucleus and to test the factorization ( $e+A/p+A/e+p/p+p$ ) of the fragmentation of par-

tons into hadrons, especially with processes involving heavy quarks. The wide photon energy available at the EIC is especially relevant as a cold matter benchmark for final states in A+A collisions at the LHC, where the typical energies of jets will be well above the maximal values available at HERMES.

**Saturation Effects in the Forward Region at RHIC and at Midrapidity at LHC** Yields of moderate  $p_T$  particles (2–4 GeV) in the forward region ( $\eta \approx 3.2$ ) of  $d+Au$  collisions at RHIC show a systematic suppression as the deuteron passes through thicker regions of the Au nucleus, as shown in Fig. 14. These particles correspond to partons of very low  $x \approx O(10^{-3} - 10^{-4})$ , suggestive of the relevance of saturation effects, especially with the large values of ( $Q_s^2 \approx 2.5-5 \text{ GeV}^2$ ) in this region. These values are comparable to those at mid-rapidity at the LHC. The theory curves shown correspond to different model assumptions. In the forward region at the LHC ( $y = 3$ ), one expects saturation momenta of order  $Q_s^2 = 10 \text{ GeV}^2$ . The establishment of saturation effects via measurements of  $G_A(x, Q^2)$  at the EIC will be vital to interpret measurements in the forward region at RHIC and at all rapidities at the LHC.

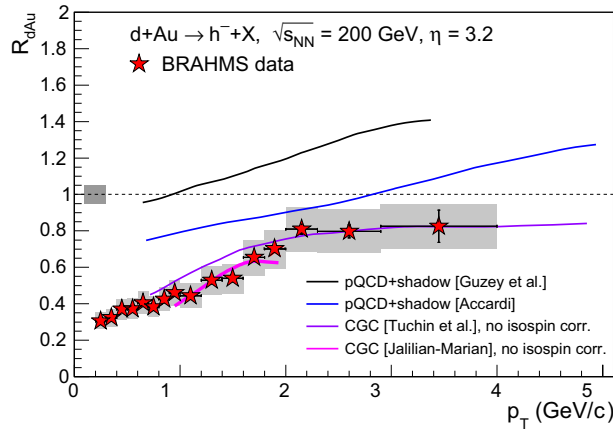


**Figure 14:** Nuclear modification factor  $R_{dAu}$ , which is the ratio between differential yield in  $d+Au$  collisions and differential cross-section in  $p+p$  collisions, scaled by the number of binary collisions, for negative charged hadrons at forward pseudorapidity.

## Collider Concepts

The requirements for an  $e+A$  collider are driven by the need to access the relevant region in  $x$  and  $Q^2$  that will allow us to explore saturation phenomena in great detail. This region is defined by our current understanding of  $Q_s(x, Q^2)$  depicted in Fig. 1. A machine that would reach sufficiently large  $Q \approx Q_s$  values in  $e+p$  collision would require energies that are beyond current budget constraints. However, as pointed out in the text box on page 9, at fixed  $x$ ,  $Q_s$  scales approximately with  $A^{1/3}$ . Ions with large masses thus allows us to reach into the saturation regime at sufficiently large  $Q$  values, which will ensure the validity of perturbative calculations. To fully explore the physics capabilities in  $e+A$ , double differential measurements at varying  $\sqrt{s}$  are mandatory. This can be only achieved if the provided beams have large luminosities.

With these considerations, one can define the following requirements for an  $e+A$  collider:

- The machine needs to provide collisions of at least  $\sqrt{s} > 60 \text{ GeV}$  to go well beyond the range explored in past fixed target experiments. The higher the energy, the longer the lever-arm in  $Q^2$  and the greater the low- $x$  reach.
- The machine must be able to provide ion beams at different energies. Measurements at various  $\sqrt{s}$  are mandatory for the study of many relevant distributions such as  $F_L$ . Note that it is kinematically better for any experimental setup to lower the ion beam energy than the electron energy.
- The machine must provide a wide range of ions. For saturation physics studies beams of very high mass numbers ( $A \geq Au$ ) are vital.
- To collect sufficient statistics luminosities with  $L > 10^{30} \text{ cm}^{-2}\text{s}^{-1}$  are required.

Since the 2001 Long Range Plan, there has been significant progress in the design of EIC accelerator concepts. There are two complementary concepts to realize EIC: (i) **eRHIC**, to construct an electron beam (either ring or linac) to collide with the existing RHIC ion complex and (ii) **ELIC**, to construct an ion complex to collide with the upgraded CEBAF accelerator.

In the next two sections we describe the current design of both concepts.

## Diffractive Deep Inelastic Scattering

Diffractive scattering, or Pomeron physics, has made a spectacular comeback with the observation of an unexpectedly large cross-section for diffractive events at the HERA  $e+p$  collider. At HERA, hard diffractive events,  $\ell(k) + N(p) \rightarrow \ell'(k') + N(p') + X$ , were observed where the proton remained intact and the virtual photon fragmented into a hard final state producing a large rapidity gap between the projectile and target devoid of particles. These events are indicative of a color singlet exchange in the t-channel between the virtual photon and the proton over several units in rapidity. This color singlet exchange has historically been called the Pomeron where the Pomeron had a specific interpretation in Regge theory. Here we will use it to denote the kinematics of the color singlet exchange without specifying the dynamics. An illustration of the hard diffractive event is shown in Fig. 15.

The kinematic variables are similar to those for DIS with the following additions:

$t = (p - p')^2$  is the square of the momentum transfer at the hadronic vertex.

$M_X^2 = (p - p' + k - k')^2$  is the diffractive mass of the final state,

$\beta = \frac{Q^2}{M_X^2 - t + Q^2}$  is the momentum fraction of the  $Q^2$  parton with respect to the Pomeron, and

$x_{\mathbb{P}} = x/\beta$  is the momentum fraction of the Pomeron with respect to the hadron.

In pQCD, the probability of a rapidity gap is exponentially suppressed as a function of the gap size  $\Delta\eta \approx \ln(1/x_{\mathbb{P}})$ . At HERA though, gaps of several units in rapidity are relatively unsuppressed; one finds that roughly 15% of the cross-section corresponds to hard diffractive events with invariant masses  $M_X > 3$  GeV. The remarkable nature of this result is transparent in the proton rest frame: a 25 TeV electron slams into the proton and  $\approx 15\%$  of the time, the proton is unaffected, even though the interaction causes the virtual photon to fragment into a hard final state. The interesting question in diffraction is the nature of the color singlet object (the ‘‘Pomeron’’) within the proton that interacts with the virtual photon. This interaction probes, in a novel fashion, the nature of confining interactions within hadrons.

The cross-section can be formulated analogously to inclusive DIS by defining the *diffractive* structure functions  $F_2^D$  and  $F_L^D$  as

$$\frac{d^4\sigma}{dx dQ^2 d\beta dt} = \frac{4\pi\alpha^2}{\beta^2 Q^4} \left[ \left(1 - y + \frac{y^2}{2}\right) F_2^{D,A}(x, Q^2, \beta, t) - \frac{y^2}{2} F_L^{D,A}(x, Q^2, \beta, t) \right]$$

In practice, detector specifics may limit measurements of diffractive events to those where the outgoing hadron is not tagged (without determining  $t$ ) requiring instead a large rapidity gap in the detector. The cross-section, formulated in terms of the structure function  $F^{D,3}$ , measures a larger cross-section than expected from simple integration,  $F^{D,3} > \int F^{D,A} dt$  because events are included where the outgoing hadron has broken up. The EIC will require careful instrumentation of forward detectors to detect intact nuclei and measure the  $t$ -dependence of diffractive events.

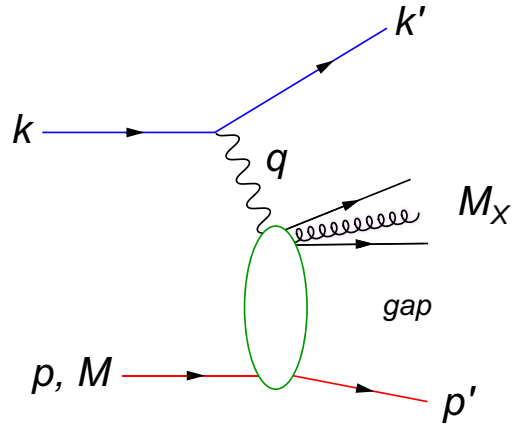
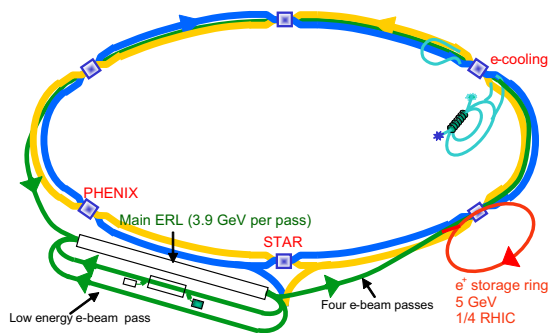


Figure 15: Kinematic quantities for the description of diffractive event.

## eRHIC

Two accelerator design options for eRHIC were developed in parallel and presented in detail in the 2004 Zeroth-Order Design Report[53]. At present, the most promising design option is based on the addition of a superconducting energy recovery linac (ERL) to the existing RHIC ion machine. The linac will provide the electron beam for the collisions with ions or protons, circulating in one of the RHIC rings. The general layout of the machine is shown in Fig. 16.



**Figure 16:** Design layout of the eRHIC collider based on the Energy Recovery Linac.

The main features of the electron machine include:

- The electron beam passes the main ERL five times during the acceleration, with the maximum energy gain per pass of 3.9 GeV. The final electron beam energy range is from 3 to 20 GeV.
- After collisions the electron beam is decelerated in the same linac. The energy recovered from the beam is used for the acceleration of subsequent electron bunches.
- The electron beam is produced by a polarized electron source and has 80% polarization degree. If needed, an unpolarized electron source can be used providing higher electron beam intensity.
- To provide a positron beam, a conversion system for the positron production may be added and a compact storage ring, at one quarter of the RHIC circumference, may be built for positron accumulation, storage and self-polarization.
- As many as four electron-ion interaction points are possible.

Another configuration is being studied (not shown) in which the whole electron ERL is located inside the RHIC tunnel. The advantage of this configuration is the reduced cost of the conventional construction. Table 1 shows the beam parameters and luminosities for  $e+Au$  collisions for highest and lowest energy setups. The luminosity integral per week is based on the average luminosity since it takes into account the luminosity deterioration during the course of the store and the time spent between stores. Due to those factors the expected average luminosity is a factor three smaller than the peak luminosity. The luminosity is proportional to the energy of ions and does not depend on the energy of electrons. R&D for the high current polarized electron source is needed to achieve the design luminosities in the ERL-based option. This R&D is not required for unpolarized electron beam. Another option of the eRHIC accelerator design under consideration is based on the addition of an electron storage ring instead of the linac. A pair of recirculating linacs of 2 GeV each provide polarized electrons or unpolarized positrons of 5 to 10 GeV which are stacked into a storage ring up to currents of 0.5–1 A. The positrons get polarized during the storage. The storage ring has one-third of the circumference of RHIC and a race-track shape with two long straight sections, one of which intersects the RHIC ring at single interaction point. The storage ring design is more mature than the ERL-based design but the achievable luminosity has additional limitations due to the deterioration of electron beam quality in the beam-beam interactions and the interaction region design issues. The design luminosities of  $e+Au$  collision for the e-ring based design is 5–10 times smaller, depending on the energy setup, than for the ERL-based design. Some upgrades have to be realized in the RHIC ion ring in order to achieve the design luminosities. Electron cooling will be required to achieve the design transverse emittances. The same electron cooling system which is presently under development for RHIC-II will be used for eRHIC. The number of ion bunches in RHIC should be increased to 166 instead of presently achieved 111.

## ELIC

Accelerator physicists at Jefferson Lab are pursuing an ELection-Ion Collider, ELIC [54], which uses the CEBAF linear accelerator and requires the construction of an ion storage ring.

	High Energy Setup		Low Energy Setup	
	Au	$e$	Au	$e$
Energy, GeV (or GeV/n)	100	20	50	3
Number of bunches	166		166	
Bunch spacing (ns)	71	71	71	71
Bunch intensity ( $10^{11}$ )	1.1	1.2	1.1	1.2
Beam current (mA)	180	260	180	260
95% normalized emittance ( $\pi$ mm mrad)	2.4	115	2.4	115
Rms emittance (nm)	3.7	0.5	7.5	3.3
$\beta$ x/y (cm)	26	200	26	60
Beam-beam parameters (x/y)	0.015	1.0	0.015	1.0
Rms bunch length (cm)	20	0.7	20	1.8
Peak Luminosity/n ( $10^{33}$ cm $^{-2}$ s $^{-1}$ )	2.9		1.5	
Luminosity integral/week /n (pb $^{-1}$ )	580		290	

**Table 1:** Luminosities and main beam parameters for  $e$ +Au collisions at eRHIC.

Ion	Ion Energy $E_A$ (GeV/n)	Luminosity at $E_e = 7$ GeV (cm $^{-2}$ s $^{-1}$ )	Luminosity at $E_e = 3$ GeV and $E_A/5$ (cm $^{-2}$ s $^{-1}$ )
Proton	150	$7.8 \cdot 10^{34}$	$6.7 \cdot 10^{33}$
Deuteron	75	$1.6 \cdot 10^{35}$	$1.3 \cdot 10^{34}$
$^3\text{H}^{+1}$	50	$2.3 \cdot 10^{35}$	$2.0 \cdot 10^{34}$
$^3\text{He}^{+2}$	100	$1.2 \cdot 10^{35}$	$1.0 \cdot 10^{34}$
$^4\text{He}^{+2}$	75	$1.6 \cdot 10^{35}$	$1.3 \cdot 10^{34}$
$^{12}\text{C}^{+6}$	75	$1.6 \cdot 10^{35}$	$1.3 \cdot 10^{34}$
$^{40}\text{Ca}^{+20}$	75	$1.6 \cdot 10^{35}$	$1.3 \cdot 10^{34}$

**Table 2:** ELIC luminosities per nucleon for  $e$ +A collisions.

ELIC is envisioned as a future upgrade of CEBAF, beyond the planned 12 GeV Upgrade for fixed target experiments. The CEBAF accelerator with the existing polarized electron source will be used as a full energy injector into an electron storage ring, capable of delivering the required electron beam energy, current, and polarization. The addition of a positron source to the CEBAF injector, will allow a positron beam to be accelerated in CEBAF, accumulated and polarized in the electron storage ring, and used in collisions with ions (and possibly electrons), with luminosity similar as for electron/ion collisions. An ion complex with a green-field design optimized to directly address the science program of ELIC, will be used to generate, accelerate, and store polarized light ions and unpolarized medium to heavy ions, and will be a major addition to the CEBAF facility.

Figure 17 displays the conceptual layout of ELIC at CEBAF. The three major constituents of ELIC are: the electron/positron complex, the ion complex with electron cooling, and the four interaction regions.

The electron/positron complex is designed to deliver electron beam in the energy range of 3 GeV

to 9 GeV, average beam current for collisions between 1 A to 3 A, and longitudinal polarization at the IP's of 80%. This electron/positron complex comprises two major facilities: the CEBAF accelerator upgraded to 12 GeV and an electron storage ring which will have to be constructed. CEBAF is a superconducting RF recirculating linac operating at the RF frequency of 1500 MHz. The 12 GeV Upgrade of CEBAF will allow energy gain of 11 GeV in five recirculations. Longitudinally polarized electrons are generated from CEBAF's polarized DC photo-injector and accelerated to the desired top energy of 3 to 9 GeV in multiple recirculations through CEBAF. They are then injected into a figure-8 shaped electron storage ring, where they are accumulated using stacking by synchrotron radiation damping.

The ion complex is designed to deliver protons in the energy range of 30 to 225 GeV and average current of 0.3 to 1 A, and light to heavy ions with maximum energy of approximately 100 GeV/n. It consists of polarized ion sources, a 200 MeV to 400 MeV linac, a pre-booster up to 3 GeV/c, and a 225 GeV, 1 A storage ring. The ion source is designed to pro-

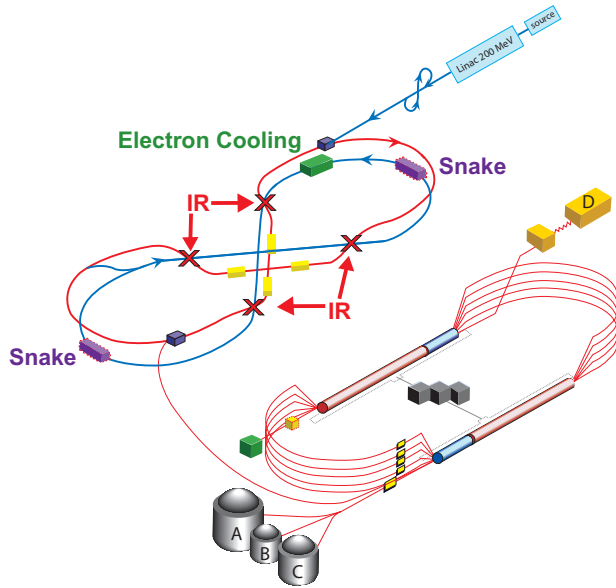


Figure 17: EIC schematic layout.

duce polarized light ion species:  $p$ ,  $d$ ,  $^3\text{He}$  and  $\text{Li}$ , and unpolarized light to heavy ion species up to  $\text{Pb}$ .

The electron ring (arcs) is used as the main, 15 to 30 GeV/u booster for the ion beam. The ion storage ring serves as the collider ring with four interaction regions. As depicted in Fig. 17, the electron and ion storage rings are designed as figure-8 shaped double rings and are housed in the same tunnel, with the ion ring below the electron ring. The rings consist of two identical arcs connected by two crossing straight beam line sections. The choice of figure-8 shape eliminates the issue of spin maintenance at acceleration and allows one to easily arrange the desired spin orientation and flipping for all the ion species at all energies.

A critical component of the ion complex is a 15 MeV to 112.5 MeV ERL-based continuous electron cooling facility, which is anticipated to provide low emittance and simultaneously very short ion bunches.

The interaction region of EIC is designed to accommodate up to four detectors simultaneously, at four collision points located symmetrically around the centers of the figure-8 colliders, along each of the two crossing straights. After beam stacking and accumulation is complete, the two storage rings are switched to the collider mode, where electron bunches are bent vertically to collide with the ion bunches. Table 2 summarizes the design peak lumi-

nosity per nucleon for  $e+A$  collisions at two different energy setups for the electron-ion collider at CEBAF. Luminosity calculations for the highest energy setups, and heavier nuclei are presently under development. Peak luminosity at the  $10^{35} \text{ cm}^{-2}\text{s}^{-1}$  level per interaction point appears feasible for 75 GeV/n ions colliding on 7 GeV electrons. EIC is designed to be compatible with simultaneous operation of the 12 GeV CEBAF for fixed target program, and its potential extension to 24 GeV.

## Experimental Concepts

A new EIC facility will require the design and construction of a new optimized detector profiting from the experience gained from the H1 and ZEUS detectors operated at the HERA collider at DESY. The details of the design will be closely coupled to the design of the interaction region, and thus to the machine development work in general.

The following minimal requirements on a future EIC detector can be made:

- Measure precisely the energy and angle of the scattered electron (Kinematics of DIS reaction)
- Measure hadronic final state (Kinematics of DIS reaction, jet studies, flavor tagging, fragmentation studies, particle ID system for heavy flavor physics and  $K/\pi$  separation)
- Missing transverse energy measurement (Events involving neutrinos in the final state, electroweak physics)

In addition to those demands on a central detector, the following forward and rear detector systems are crucial:

- Zero-degree photon detector to control radiative corrections and measure Bremsstrahlung photons for luminosity measurements (absolute and relative with respect to different  $e+p$  spin combinations)
- Tag electrons under small angles ( $< 1^\circ$ ) to study the non-perturbative and perturbative QCD transition region
- Tagging of forward particles (Diffraction and nuclear fragments)

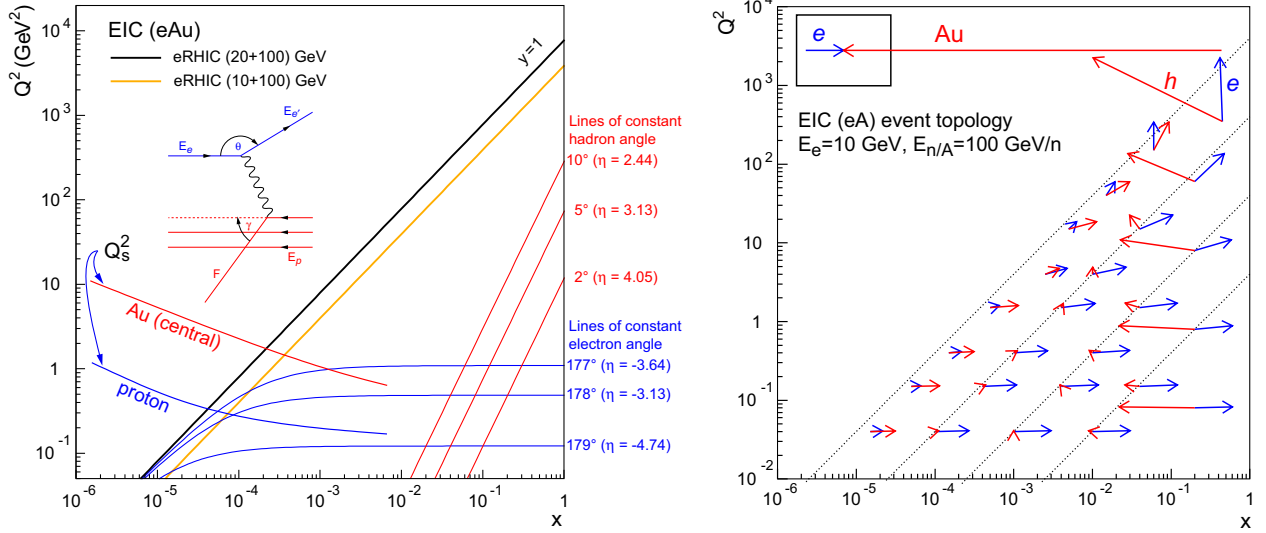


**Figure 18:** Kinematic  $Q^2$ - $x$  plane for  $E_e = 10$  (20) GeV and  $E_A = 100$  GeV. Left: Shown are the lines of constant electron scattering angles (blue) for  $\theta = 177^\circ$ ,  $178^\circ$ , and  $179^\circ$ , as well as the hadron/jet scattering angles  $\gamma = 2^\circ$ ,  $5^\circ$ , and  $10^\circ$ . Note that for many measurements (e.g.  $F_2$ ) the reconstruction of the event kinematic at low- $x$  is best done using the scattered electron, while at large  $x$  the reconstruction of the final hadronic state is more precise (Jacquet-Blondel method). Right: shows the direction and energy of the scattered electron and current jet. The scale is taken with respect to the incoming electron and proton beams shown on the upper left corner [55].

Fig. 18 shows the kinematic  $Q^2 - x$  plane for  $E_e = 10$  GeV (20 GeV) and  $E_A = 100$  GeV with the direction and energy of the scattered electron and current jet for several  $(Q^2, x)$  points. In the low- $Q^2$  / low- $x$  region both the scattered electron and current jet are found mainly in the rear direction with energies well below 10 GeV. Good electron/hadron separation is essential. As  $x$  grows, the current jet moves forward with larger energies and is clearly separated from the scattered electron at low- $Q^2$ . At high- $Q^2$  / high- $x$  both the current jet and the scattered electron are found mainly in the barrel and forward direction with energies much larger than 10 GeV (electron) and 100 GeV (current-jet).

Optimizing all of these requirements is a challenging task. Two detector concepts have been considered so far. One, which focuses on the rear/forward acceptance (Fig. 19) and thus on low- $x$ /high- $x$  physics, which emerges out of the HERA-III detector studies [56]. This detector concept is based on a compact system of tracking and central electromagnetic calorimetry inside a magnetic dipole field and calorimetric end-walls outside. Forward produced charged particles are bent into the detector volume which extends the rapidity coverage compared to existing detectors.

The design shown in Fig. 20 is a wide acceptance detector similar to the current HERA collider experiments H1 and ZEUS [55]. The physics program demands high luminosity and focusing machine elements in a ring-ring configuration have to be as close as possible to the interaction region while preserving good central detector acceptance. The hermetic inner and outer tracking system and the electromagnetic section of the barrel calorimeter is surrounded by an axial magnetic field. The forward calorimeter is divided into hadronic and electromagnetic sections. The rear and barrel electromagnetic calorimeter consists of segmented towers, e.g., a W-Si type. This would result in a compact configuration. A future EIC facility with only one interaction region will be challenged to combine both of the above detector concepts to maximize its physics reach.

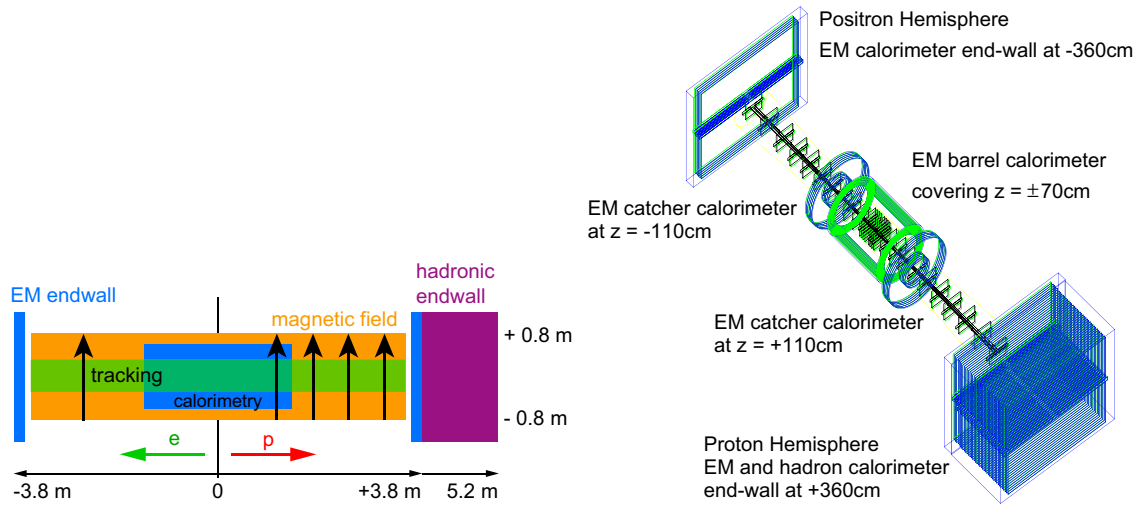


**Figure 19:** Concept of a detector layout focusing on forward physics. Left: Conceptual layout of the detector with a 7m long dipole field and an interaction region without machine elements extending from -3.8 m to +5.2 m. Right: Schematic overview over the detector components within  $\approx \pm 5$  m of the interaction point. The silicon planes are visible inside the yellow tracking volume. The calorimeter system consisting of a central barrel, a catcher ring on each side and end-walls is depicted in blue and green. From [56].

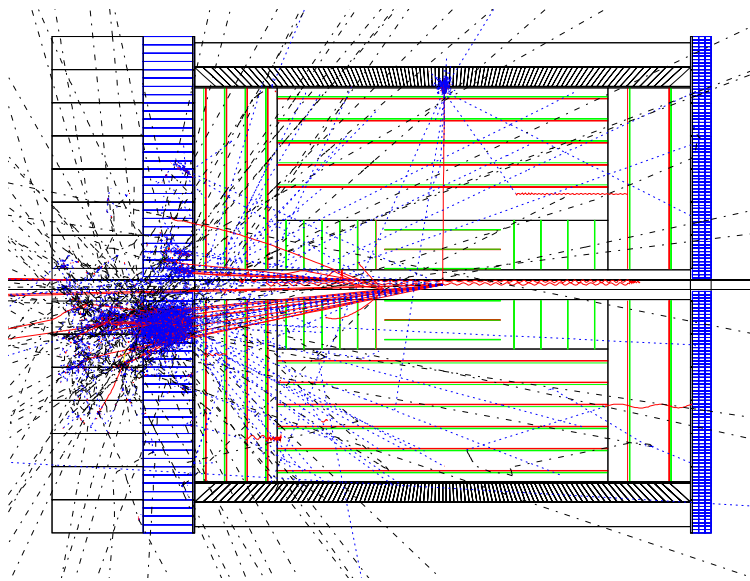


**Figure 20:** Schematic layout of a design focusing on a wide acceptance detector system similar to the current HERA collider experiments H1 and ZEUS to allow for the maximum possible  $Q^2$  range. Depicted is the side view of the GEANT detector implementation as part of the ELECTRA simulation and reconstruction package. A deep-inelastic scattering event resulting from a LEPTO simulation is overlaid with  $Q^2 = 361 \text{ GeV}^2$  and  $x = 0.45$ . From [55].

## References

- [1] E. Iancu and R. Venugopalan. The color glass condensate and high energy scattering in QCD. 2003, hep-ph/0303204.
- [2] H. Weigert. Evolution at small x: The color glass condensate. *Prog. Part. Nucl. Phys.*, 55:461–565, 2005, hep-ph/0501087.
- [3] A. Donnachie and P.V. Landshoff. *Phys. Lett. B*, 437:408, 1998.
- [4] N. Armesto. *J. Phys. G*, 32:R367, 2006, hep-ph/0604108.
- [5] B. W. Harris and J. Smith. *Phys. Rev. D*, 57:2806, 1998.
- [6] Mark A. Bell. Beauty and charm physics at HERA. 2006, hep-ex/0602032.
- [7] Jeannine Wagner. Charm production in e+p collisions. 2005, hep-ex/0505078.
- [8] B. W. Harris, J. Smith, and R. Vogt. *Nucl. Phys. B*, 461:181, 1996.
- [9] M. Arneodo, A. Bialas, M. W. Krasny, T. Sloan, and M. Strikman. Nuclear beams in HERA. 1996, hep-ph/9610423.
- [10] S. Brodsky et al. *Phys. Rev. D*, 50:3134, 1994.
- [11] L. Frankfurt, V. Guzey, M. McDermott, and M. Strikman. *Phys. Rev. Lett.*, 87:192301, 2001.
- [12] S. Munier, A. M. Stasto, and A. H. Mueller. *Nucl. Phys. B*, 603:427, 2001.
- [13] T. Rogers, V. Guzey, M. Strikman, and X. Zu. *Phys. Rev. D*, 69:074011, 2004.
- [14] H. Kowalski, L. Motyka, and G. Watt. *Phys. Rev. D*, 74:074016, 2006.
- [15] H. Kowalski and D. Teaney. *Phys. Rev. D*, 68:114005, 2003.
- [16] N. Armesto, C. A. Salgado, and U. A. Wiedemann. *Phys. Rev. Lett.*, 94:022002, 2005.
- [17] A. Freund and M. Strikman. *Phys. Rev. C*, 69:015203, 2004, hep-ph/0307211.
- [18] A. Freund and M. Strikman. *Eur. Phys. J. C*, 33:53, 2004, hep-ph/0309065.
- [19] M. V. Polyakov. Generalized parton distributions and strong forces inside nucleons and nuclei. *Phys. Lett.*, B555:57–62, 2003, hep-ph/0210165.
- [20] V. Guzey and M. Siddikov. On the A-dependence of nuclear generalized parton distributions. *J. Phys.*, G32:251–268, 2006, hep-ph/0509158.
- [21] V. Guzey and M. Strikman. DVCS on spinless nuclear targets in impulse approximation. *Phys. Rev.*, C68:015204, 2003, hep-ph/0301216.
- [22] K. Golec-Biernat and M. Wusthoff. *Phys. Rev.*, D59:014017, 1999.
- [23] A. H. Mueller and D. N. Triantafyllopoulos. *Nucl. Phys.*, B640:331, 2002.
- [24] M. S. Kugeratski, V. P. Goncalves, and F. S. Navarra. *Eur. Phys. J. C*, 46:413, 2006.
- [25] N. Armesto, A. Capella, A. B. Kaidalov, J. Lopez-Albacete, and C. A. Salgado. *Eur. Phys. J. C*, 29:531, 2003.
- [26] L. S. Osborne et al. *Phys. Rev. Lett.*, 40:1624, 1978.

- [27] J. Ashman et al. *Z. Phys. C*, 52, 1991.
- [28] A. Airapetian et al. *Phys. Lett. B*, 577:37, 2003, hep-ex/0307023.
- [29] W. K. Brooks. *FizikaB*, 13:321, 2004, nucl-ex/0310032.
- [30] W. K. Brooks. talk at Jefferson Laboratory Users Group Workshop, 2006.
- [31] First three years of operation of RHIC. *Nucl. Phys. A*, 757(1–2):1–283, 2005.
- [32] A. Accardi. Can we distinguish energy loss from hadron absorption? *Acta Phys. Hung.*, A27:189–192, 2006, nucl-th/0510090.
- [33] E. Wang and X. N. Wang. *Phys. Rev. Lett.*, 89:162301, 2002.
- [34] F. Arleo. *JHEP*, 0211:044, 2002.
- [35] F. Arleo. *Eur. Phys. J. C*, 30:213, 2003.
- [36] W. Cassing, T. Falter, K. Gallmeister, and U. Mosel. *Phys. Rev. C*, 70:054609, 2004.
- [37] B. Z. Kopeliovich, J. Nemchik, and I. Schmidt, hep-ph/0608044.
- [38] A. Bialas and M. Gyulassy. *Nucl. Phys. B*, 291:793, 1987.
- [39] J. W. Qiu and I. Vitev. *Phys. Rev. Lett.*, 93:262301, 2004, hep-ph/0309094.
- [40] J.C. Collins, D.E. Soper, and G. Sterman. *Adv. Ser. Direct. High Energy Phys.*, 5:1, 1988.
- [41] R. Doria, J. Frenkel, and J. C. Taylor. *Nucl. Phys. B*, 168:93, 1980.
- [42] C. Di’Lieto, S. Gendron, I. G. Halliday, and C. T. Sachrajda. *Nucl. Phys. B*, 183:223, 1981.
- [43] J. W. Qiu and G. Sterman. *Nucl. Phys. B*, 353:137, 1991.
- [44] F. P. Schilling. *Acta Phys. Polon. B*, 33:3419, 2002, hep-ex/0209001.
- [45] M. Gyulassy and L. McLerran. *Nucl. Phys. A*, 750:30, 2005.
- [46] A. Krasnitz and R. Venugopalan. *Phys. Rev. Lett.*, 86:1717, 2001.
- [47] D. Kharzeev and M. Nardi. *Phys. Lett. B*, 507:121, 2001.
- [48] D. Kharzeev and E. Levin. *Phys. Lett. B*, 523:79, 2001.
- [49] R. Baier, A. H. Mueller, D. Schiff, and D. T. Son. *Phys. Lett. B*, 502:51, 2001.
- [50] S. Mrowczynski and M. H. Thoma, nucl-th/0701002.
- [51] T. Hirano and Y. Nara. *Nucl. Phys. A*, 743:305, 2004.
- [52] M. Djordjevic. *J. Phys. G*, 32:S333, 2006, nucl-th/0610054.
- [53] eRHIC zeroth-order design report, 2004. Editors: M. Farkhondeh and V. Ptitsyn, BNL CA-D Note 142.
- [54] Zero<sup>th</sup> order design report for the electron-ion collider at CEBAF, 2007. Editors: Ya. Derbenev, L. Mermininga, Y. Zhang.
- [55] B. Surrow. eRHIC: Accelerator and detector design studies. 2006, physics/0608290.
- [56] I. Abt, A. Caldwell, X. Liu, and J. Sutiak. A detector for forward physics at eRHIC: Feasibility study. 2004, hep-ex/0407053.